Brain Tumor Pathol (2011) 28:71–76
DOI 10.1007/s10014-010-0008-y

CASE REPORT

A case of atypical teratoid/rhabdoid tumor in an adult, with long survival

Kenta Takahashi · Hiroshi Nishihara · Masahito Katoh · Tomoaki Yoshinaga · Roshan Mahabir · Hiromi Kanno · Taichi Kimura · Mishie Tanino · Jun Ikeda · Yutaka Sawamura · Kazuo Nagashima · Shinya Tanaka

Received: 6 September 2010 / Accepted: 5 October 2010 / Published online: 23 December 2010

Abstract Atypical teratoid/rhabdoid tumor (AT/RT) is a malignant tumor that mostly occurs in early childhood and has poor prognosis despite aggressive therapy. Adult cases are rare and, as far as we are aware, only 30 cases have been reported to date. Here we present the case of a 27-year-old female with left parietal AT/RT with the chief complaint of numbness of the right superior limb. First, the tumor was surgically removed and the diagnosis was grade II glioma. With additional radiotherapy, the clinical course after surgery was favorable. After 6 years, she had an operation for recurrence and the diagnosis was grade III glioma. Temozolomide was prescribed, and a disease-free period of 2 years followed. Surgery was performed for a third time for second recurrence with histology of diffuse growth of rhabdoid cells. Immunohistochemistry was partially positive for vimentin and epithelial membrane antigen. Ki-67 labeling index was extremely high and tumor cells showed no staining of INI1 suggestive of diagnosis of AT/RT. We re-evaluated past specimens and none had immunoreactivity of INI1. Ki-67 labeling index and O-6 methylguanine DNA methyltransferase (MGMT) staining were also re-examined and both increased gradually. She is still alive without recurrence for more than 1 year. As far as we are aware, this is the second longest survival of an adult with AT/RT.

Keywords Atypical teratoid/rhabdoid tumor · Adult · Long survival · INI1 · O-6 methylguanine DNA methyltransferase · Immunohistochemistry

Introduction

Atypical teratoid rhabdoid tumor (AT/RT) is a highly malignant tumor of the central nervous system which mostly occurs in children younger than 3 years old [1–5]. This entity was established in the late 1990s by demonstration of mutation of INI1/hSNF5 (HIV-integrase interactor 1/human homolog of *Saccharomyces cerevisiae* sucrose-nonfermenting gene 5) [6–11]. Symptoms depend on its location, and surgical removal is the most important therapy. Despite additional radiation and chemotherapy, the prognosis is usually poor. Histologically this tumor has scattered growth of rhabdoid cells with round to oval-shaped nuclei, prominent nucleoli, and eosinophilic cytoplasm occasionally with inclusion like components. Primitive neuroepithelial, epithelial, and mesenchymal components are also observed. Immunohistochemical

---

K. Takahashi · T. Yoshinaga · R. Mahabir · H. Kanno · T. Kimura · M. Tanino · S. Tanaka (✉)
Laboratory of Cancer Research, Department of Pathology, Hokkaido University Graduate School of Medicine,
N15, W7, Kita-Ku, Sapporo, Hokkaido, Japan
e-mail: tanaka@med.hokudai.ac.jp

H. Nishihara · S. Tanaka
Department of Translational Pathology,
Hokkaido University Graduate
School of Medicine, Sapporo, Japan

M. Katoh
Hokkaido Neurosurgical Memorial Hospital, Sapporo, Japan

J. Ikeda
Sapporo IGRT Clinic, Sapporo, Japan

Y. Sawamura
Department of Neurosurgery,
Hokkaido University Graduate School of Medicine,
Sapporo, Japan

K. Nagashima
Department of Pathology, Sapporo Higashi-Tokushukai
Hospital, Sapporo, Japan

examination reveals favored staining of epithelial membrane antigen (EMA) and vimentin, sometimes glial fibrillary acidic protein (GFAP). The percentage Ki-67 labeling index is high. Diagnosis is confirmed by negative staining of INI1. This tumor rarely occurs in adults and only 30 adult (older than 18 years old) cases have been reported [12–35]. Here we report a case of brain tumor in a 27-year-old female who had long survival. Diagnosis of AT/RT was confirmed by immunohistochemistry. The status of O-6 methylguanine DNA methyltransferase (MGMT) was also examined.

Clinical summary

A 27-year-old female visited the neurosurgeon because of numbness of her right upper limb. She had no past history of such a symptom and her family history had nothing particular. Radiological examination showed an intraaxial mass on her left parietal lobe (data not shown). The lesion was completely removed surgically. Based on the pathological diagnosis of grade II glioma, she had additional radiotherapy of 54 Gy/27 Fr. At 33 years old, after a disease-free period of 6 years, she had recurrence of a well enhanced tumor as seen by magnetic resonance imaging (MRI) (Fig. 1a). The surgically resected tumor was diagnosed as grade III glioma by the pathologist. After second surgery, chemotherapy with temozolomide was started and then she lived for 2 years with no disability. When she was 35 years of age, again there was recurrence at the same location (Fig. 1b). With a third operation, the tumor was excised. Currently, 9 years after her first operation, she has no further recurrences and no problems in her daily life. Pathological examination of the resected tumor with review of past specimens was performed with additional immunohistochemistry examining the entire course of the progression of this tumor.

Pathological findings

Morphological findings by hematoxylin and eosin (H&E) stain

The primary tumor had two types of components (Fig. 2a, b). One was tumor cells with a background of eosinophilic pilocytic cells; tumor cells had dense atypical nuclei with little cytoplasm. The other part showed diffuse growth of tumor cells with mucinous background; tumor cells had relatively little connection each other and nuclei were round to oval shaped with atypia. In some tumor cells, the eosinophilic cytoplasm seemed to be pushing the nucleus aside.

Compared with the first specimen, the recurrent tumor cells had much higher cellularity and nuclear/cytoplasm ratio and close proliferation with narrow intracellular spaces (Fig. 2c). Mitotic figures were seen in many fields and nuclei were round to oval shaped with prominent nucleoli. Some parts also showed a mucinous background similar to the first specimen.

Like the past tumors, the second recurrent neoplastic cells increased diffusely with mucinous, focally chondroid background (Fig. 2d). Nuclei were round to oval shaped in most cells with obvious atypia. Because nuclei showed maldistribution in eosinophilic cytoplasm, which had inclusion-like structures in some cells, the tumor cells looked like rhabdoid ones. Precise epithelial and neuroepithelial components were not seen.

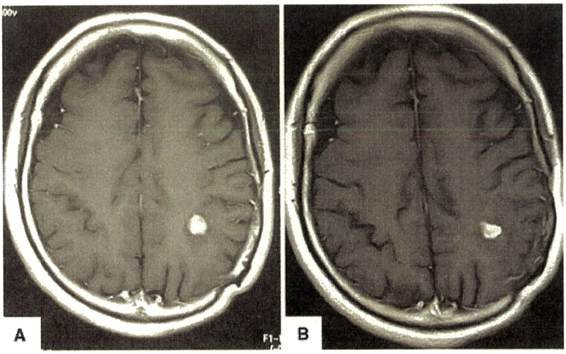

Fig. 1 T1-weighted axial magnetic resonance image (MRI) with contrast enhancement shows a left parietal tumor. **a** Tumor imaging of the first recurrence. Patient was 33 years old. **b** Second recurrence when she was 35 years old

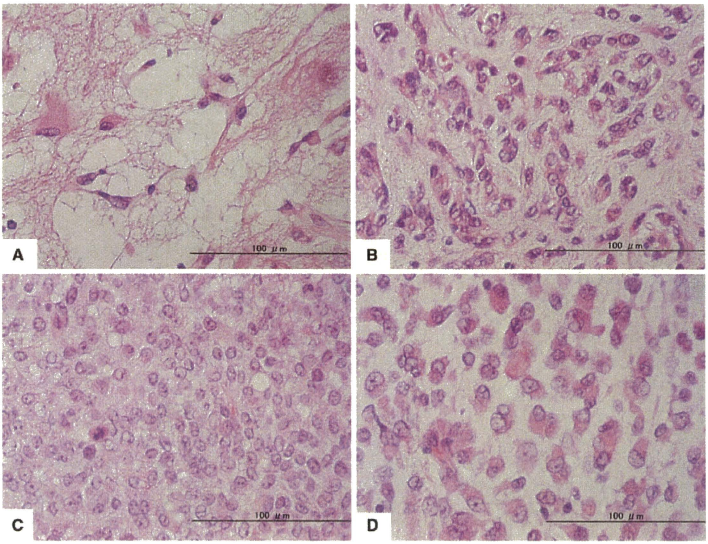

Fig. 2 H&E staining of the tumor. **a**, **b** Two components of the first tumor when the patient was 27 years old. **c** Recurrent tumor when she was 33 years old. **d** Second recurrent tumor when she was 35 years old

Table 1 Immunohistochemistry of tumor cells

Antibodies	Primary	First recurrence	Second recurrence
GFAP	–	–	–
Vimentin	+	+	+
EMA	+	–	+
Ki-67	1%	20%	50%
MGMT (0–3+)	1+	3+	3+
INI-1	–	–	–

Immunohistochemical findings

The primary tumor immunohistochemistry showed the same tendency for both components. There was no staining of tumor cells for GFAP and Olig2, but focal positivity for vimentin and EMA were confirmed. The Ki-67 labeling index was only 1% of all tumor cells; in the first and second recurrent tumors it was 20 and 50%, respectively (Table 1; Fig. 3). Immunoreactivity of the first recurrent tumor was the same as for the first specimen, except for EMA. The second recurrent tumor was partially positive only for vimentin and EMA. MGMT was evaluated this time and was strongly positive in most tumor cells. The presence of rhabdoid tumor cells led us to try immunostaining of INI-1; tumor cells were totally negative for INI1, which led to diagnosis of AT/RT. We confirmed the past tumor cells were also INI1 negative. This finding revised the former diagnosis of glioma and the tumor was regarded as AT/RT from the beginning. Additional staining of MGMT showed weak staining for the first specimen and stronger positivity for the second.

Discussion

AT/RT is a highly malignant tumor mostly occurring in early childhood, with poor prognosis [1–5]. Here we present an unusual case of AT/RT with adult onset and more than 9 years survival. To our knowledge, this is the 31st case of adult AT/RT and the second longest adult survival [12–35]. In the literature, some cases of adult AT/RT have better prognosis than infant cases. This may be partly because of adult resilience and the use of stronger radiation and more potent chemotherapy. Otherwise some adult AT/RT cases may have a different unknown biological nature in comparison with most infant cases.

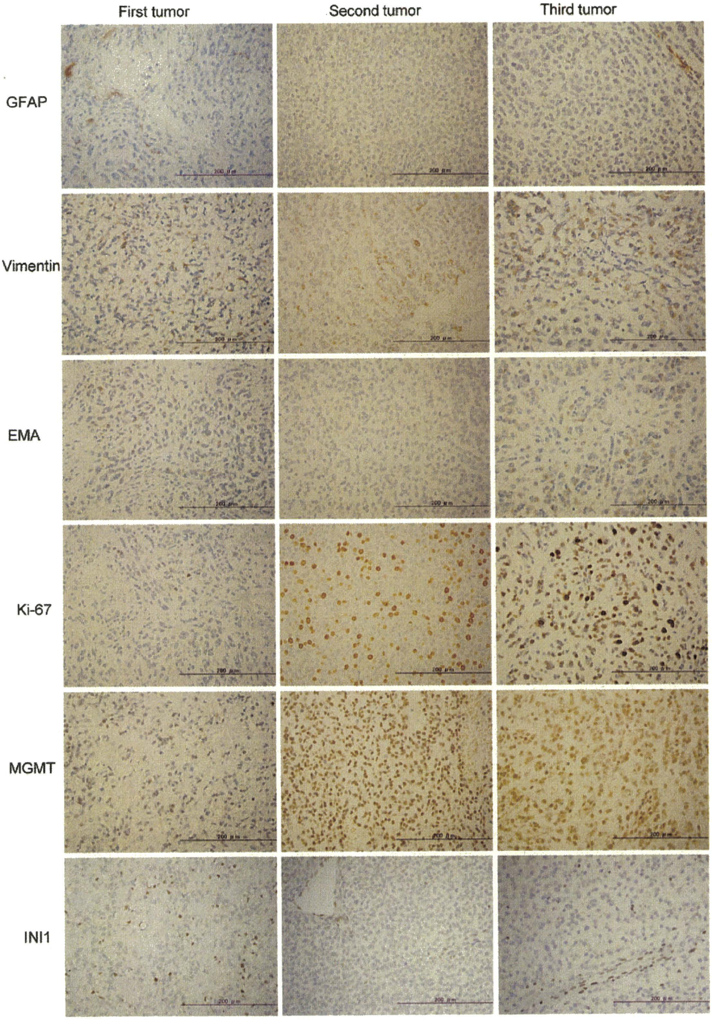

Fig. 3 Histopathologic characteristics of immunohistochemistry

First and second pathological diagnosis was revised this time and INI1 immunostaining helped and supported this process. Although the first specimen had a glioma-like structure in some parts and low Ki-67 index, immunohistochemistry did not support the diagnosis of glioma, especially because INI1 was clearly negative.

In addition to these facts, this is the first report of adult AT/RT evaluated with MGMT, following the course from the beginning, Ki-67 labeling index and MGMT staining increased. On the basis that this tumor was AT/RT when this patient had her first surgery, it seemed to acquire high proliferative ability and resistance to therapies during the course of 9 years.

This is a case report of adult onset of AT/RT with long survival after surgery and adjuvant therapy. Although AT/RT is a rare tumor in adults, INI1 immunohistochemistry is a powerful tool for diagnosis. Thus appropriate immunohistochemical evaluation should be performed to diagnose this small number of cases and shows us the most suitable way for future therapy.

Acknowledgments We thank Eiko Aoyanagi, Miho Nodagashira, and Kazuko Shimizu for their excellent technique. This study is supported by the grant from Ministry of Education, Culture, Sports, Science, and Technology, Japan.

References

1. Lefkowitz IB, Rorke LB, Packer RJ (1987) Atypical teratoid tumor of infancy: definition of an entity. Ann Neurol 22:448–449
2. Rorke LB, Packer RJ, Biegel JA et al (1996) Central nervous system atypical teratoid/rhabdoid tumors of infancy and childhood: definition of an entity. J Neurosurg 85:56–65
3. Burger PC, Yu IT, Tihan T et al (1998) Atypical teratoid/rhabdoid tumor of the central nervous system: a highly malignant tumor of infancy and childhood frequently mistaken for medulloblastoma: a Pediatric Oncology Group study. Am J Surg Pathol 22:1083–1092
4. Reddy AT (2005) Atypical teratoid/rhabdoid tumors of the central nervous system. J Neurooncol 75:309–313
5. Biswas A, Goyal S, Puri T et al (2009) Atypical teratoid rhabdoid tumor of the brain: case series and review of literature. Childs Nerv Syst 25:1495–1500
6. Biegel JA, Rorke LB, Packer RJ et al (1990) Monosomy 22 in rhabdoid or atypical tumors of the brain. J Neurosurg 73:710–714
7. Versteege I, Sévenet N, Lange J et al (1998) Truncating mutations of hSNF5/INI1 in aggressive paediatric cancer. Nature 394:203–206
8. Biegel JA, Zhou JY, Rorke LB et al (1999) Germ-line and acquired mutations of INI1 in atypical teratoid and rhabdoid tumors. Cancer Res 59:74–79
9. Rousseau-Merck MF, Versteege I, Legrand I et al (1999) hSNF5/INI1 inactivation is mainly associated with homozygous deletions and mitotic recombinations in rhabdoid tumors. Cancer Res 59:3152–3156
10. Biegel JA, Kalpana G, Knudsen ES et al (2002) The role of INI1 and the SWI/SNF complex in the development of rhabdoid tumors: meeting summary from the workshop on childhood atypical teratoid/rhabdoid tumors. Cancer Res 62:323–328
11. Judkins AR, Mauger J, Rorke LB et al (2004) Immunohistochemical analysis of hSNF5/INI1 in pediatric CNS neoplasms. Am J Surg Pathol 28:644–650
12. Horn M, Schlote W, Lerch KD et al (1992) Malignant rhabdoid tumor: primary intracranial manifestation in an adult. Acta Neuropathol 83:445–448
13. Cossu A, Massarelli G, Manetto V et al (1993) Rhabdoid tumours of the central nervous system. Report of three cases with immunocytochemical and ultrastructural findings. Virchows Arch A Pathol Anat Histopathol 422:81–85
14. Fisher BJ, Siddiqui J, Macdonald D et al (1996) Malignant rhabdoid tumor of brain: an aggressive clinical entity. Can J Neurol Sci 23:257–263
15. Ashraf R, Bentley RC, Awan AN et al (1997) Implantation metastasis of primary malignant rhabdoid tumor of the brain in an adult (one case report). Med Pediatr Oncol 28:223–227
16. Byram D et al (1998) (1999) Regarding Weiss, IJROBP 41: 103–109. Int J Radiat Oncol Biol Phys 45:247
17. Sugita Y, Takahashi Y, Hayashi I et al (1999) Pineal malignant rhabdoid tumor with chondroid formation in an adult. Pathol Int 49:1114–1118
18. Kuge A, Kayama T, Tsuchiya D et al (2000) Suprasellar primary malignant rhabdoid tumor in an adult: a case report (in Japanese). No Shinkei Geka 28:351–358
19. Arrazola J, Pedrosa I, Méndez R et al (2000) Primary malignant rhabdoid tumour of the brain in an adult. Neuroradiology 42:363–367
20. Lutterbach J, Liegibel J, Koch D et al (2001) Atypical teratoid/rhabdoid tumors in adult patients: case report and review of the literature. J Neurooncol 52:49–56
21. Bruch LA, Hill DA, Cai DX et al (2001) A role for fluorescence in situ hybridization detection of chromosome 22q dosage in distinguishing atypical teratoid/rhabdoid tumors from medulloblastoma/central primitive neuroectodermal tumors. Hum Pathol 32:156–162
22. Pimentel J, Silva R, Pimentel T (2003) Primary malignant rhabdoid tumors of the central nervous system: considerations about two cases of adulthood presentation. J Neurooncol 61:121–126
23. Kachhara R, Retnam TM, Kumar S et al (2003) Rhabdoid tumor of the thalamus. Neurol India 51:273–274
24. Kawaguchi T, Kumabe T, Watanabe M et al (2004) Atypical teratoid/rhabdoid tumour with leptomeningeal dissemination in an adult. Acta Neurochir (Wien) 146:1033–1038 (discussion 1038)
25. Erickson ML, Johnson R, Bannykh SI et al (2005) Malignant rhabdoid tumor in a pregnant adult female: literature review of central nervous system rhabdoid tumors. J Neurooncol 74:311–319
26. Raisanen J, Biegel JA, Hatanapaa KJ et al (2005) Chromosome 22q deletion in atypical teratoid/rhabdoid tumors in adults. Brain Pathol 15:23–28
27. Chen YW, Wong TT, Ho DM et al (2006) Impact of radiotherapy for pediatric CNS atypical teratoid/rhabdoid tumor (single institute experience). Int J Radiat Oncol Biol Phys 64:1038–1043
28. Rezanko T, Tunakan M, Kaharaman A et al (2006) Primary rhabdoid tumor of the brain in an adult. Neuropathology 26:57–61
29. Ingold B, Moschopulos M, Hutter G et al (2006) Abdominal seeding of an atypical teratoid/rhabdoid tumor of the pineal gland along a ventriculoperitoneal shunt catheter. Acta Neuropathol 111:56–59
30. Chacko G, Chacko AG, Dunham CP et al (2007) Atypical teratoid/rhabdoid tumor arising in the setting of a pleomorphic xanthoastrocytoma. J Neurooncol 84:217–222

31. Zarovnaya EL, Pallatroni HF, Hug EB et al (2007) Atypical teratoid/rhabdoid tumor of the spine in an adult: case report and review of the literature. J Neurooncol 84:49–55
32. Arita K, Sugiyama K, Sano T et al (2008) Atypical teratoid/rhabdoid tumor in sella turcica in an adult. Acta Neurochir (Wien) 150:491–495 (discussion 496)
33. Makuria AT, Rushiing EJ, McGrail KM et al (2008) Atypical teratoid rhabdoid tumor (AT/RT) in adults: review of four cases. J Neurooncol 88:321–330
34. Samaras V, Stamatelli A, Samaras E et al (2009) Atypical teratoid/rhabdoid tumor of the central nervous system in an 18-year-old patient. Clin Neuropathol 28:1–10
35. Takei H, Adesina AM, Mehta V et al (2010) Atypical teratoid/rhabdoid tumor of the pineal region in an adult. J Neurosurg 113:374–379

Biomaterials 32 (2011) 3106–3114

Contents lists available at ScienceDirect

Biomaterials

journal homepage: www.elsevier.com/locate/biomaterials

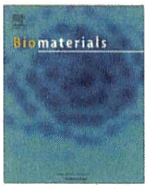

Enhanced endosomal escape of siRNA-incorporating hybrid nanoparticles from calcium phosphate and PEG-block charge-conversional polymer for efficient gene knockdown with negligible cytotoxicity

Frederico Pittella [a], Mingzhen Zhang [b,d], Yan Lee [b,e], Hyun J. Kim [b], Theofilus Tockary [b], Kensuke Osada [b], Takehiko Ishii [a], Kanjiro Miyata [c], Nobuhiro Nishiyama [c], Kazunori Kataoka [a,b,c,*]

[a] *Department of Bioengineering, Graduate School of Engineering, The University of Tokyo, 7-3-1 Hongo, Bunkyo-ku, Tokyo 113-8656, Japan*
[b] *Department of Materials Engineering, Graduate School of Engineering, The University of Tokyo, 7-3-1 Hongo, Bunkyo-ku, Tokyo 113-8656, Japan*
[c] *Center for Disease Biology and Integrative Medicine, Graduate School of Medicine, The University of Tokyo, 7-3-1 Hongo, Bunkyo-ku, Tokyo 113-0033, Japan*
[d] *School of Ophthalmology and Optometry, Wenzhou Medical College, Wenzhou, Zhejiang 325027, PR China*
[e] *Department of Chemistry, College of Natural Science, Seoul National University, Seoul 151-747, Republic of Korea*

ARTICLE INFO

Article history:
Received 4 December 2010
Accepted 31 December 2010
Available online 26 January 2011

Keywords:
Calcium phosphate nanoparticles
Endosomal escape
Vascular endothelial growth factor (VEGF)
siRNA
Charge-conversional polymer (CCP)
Poly(ethylene glycol) (PEG)

ABSTRACT

Development of safe and efficient short interfering RNA (siRNA) delivery system for RNA interference (RNAi)-based therapeutics is a current critical challenge in drug delivery field. The major barriers in siRNA delivery into the target cytoplasm are the fragility of siRNA in the body, the inefficient cellular uptake, and the acidic endosomal entrapment. To overcome these barriers, this study is presenting a hybrid nanocarrier system composed of calcium phosphate comprising the block copolymer of poly(ethylene glycol) (PEG) and charge-conversional polymer (CCP) as a siRNA vehicle. In these nanoparticles, the calcium phosphate forms a stable core to incorporate polyanions, siRNA and PEG–CCP. The synthesized PEG–CCP is a non-toxic endosomal escaping unit, which induces endosomal membrane destabilization by the produced polycation through degradation of the flanking *cis*-aconitylamide of CCP in acidic endosomes. The nanoparticles prepared by mixing of each component was confirmed to possess excellent siRNA-loading efficiency (~80% of dose), and to present relatively homogenous spherical shape with small size. With negligible cytotoxicity, the nanoparticles efficiently induced vascular endothelial growth factor (VEGF) mRNA knockdown (~80%) in pancreatic cancer cells (PanC-1). Confocal laser scanning microscopic observation revealed rapid endosomal escape of siRNA with the nanoparticles for the excellent mRNA knockdown. The results obtained demonstrate our hybrid nanoparticle as a promising candidate to develop siRNA therapy.

1. Introduction

Since the finding of RNA interference (RNAi) in 1998 [1], the scientific community has experienced the excitement to develop a new research field. Short interfering RNA (siRNA), which allows the cleavage of the complementary mRNA for the reduced protein production in mammalian cells, provided new perspectives for potential treatment of intractable and genetic related diseases [2]. With the decoding of the human genome [3–5], it has become possible to aim a great variety of genes involved in key pathways of physiopathologies. However, a safe and efficient delivery of siRNA into the target cytoplasm has still been a major challenge. Naked siRNAs are susceptible to enzymatic degradation in the body and also possess large size (~13 kDa) and anionic charges suppressing the penetration into cellular membrane [6], thus requiring carrier systems to overcome these barriers.

Calcium phosphate (CaP) precipitates were used as transfection reagents of viral DNA for the first time in early 1970s [7], as they are believed to be non-toxic based on homology to natural inorganic materials such as teeth and bones. Notably, CaP precipitates can bind and encapsulate polyanions/nucleic acids by an easy and inexpensive method to protect the nucleic acids from enzymatic degradation and to deliver into cells. However, one of their major limitations is the uncontrollable rapid growth of calcium phosphate crystal after preparation, resulting in the formation of large agglomerates (>μm) to appreciably reduce the transfection efficiency [8–10]. In this regard, our previous studies have addressed poly(ethylene glycol) (PEG)-coating of CaP precipitates utilizing PEG-polyanion block copolymers [9,11–14]. Hydrophilic and neutral PEG is widely known

---

* Corresponding author. Department of Bioengineering, Graduate School of Engineering, The University of Tokyo, 7-3-1 Hongo, Bunkyo-ku, Tokyo 113-8656, Japan.
E-mail address: kataoka@bmw.t.u-tokyo.ac.jp (K. Kataoka).

0142-9612/$ – see front matter © 2011 Elsevier Ltd. All rights reserved.
doi:10.1016/j.biomaterials.2010.12.057

to provide a nanoparticle with excellent colloidal stability as well as reduced protein adsorption and immunogenicity [15–17]. Indeed, the integration of PEG-block polyanions, such as poly(aspartic acid) (PAsp) [9,12], poly(methacryl acid) [13], and siRNA [14], into CaP precipitates led to the formation of size-controllable hybrid nanoparticles with PEG palisade, which appreciably facilitated the internalization of nucleic acids by cells.

Herein, we considered the next challenge in the CaP carriers as the endosomal escape, since they are usually internalized by cells though endocytosis pathway to be delivered into acidic endosome or lysosome, resulting in enzymatic degradation of the payload nucleic acids [18]. Toward the endosomal escape with polymeric materials, our previous studies have reported a cationic polyaspartamide with a 1,2-diaminoethane side chain (poly{*N*-[*N*′-(2-aminoethyl)-2-aminoethyl] aspartamide}, PAsp(DET)) to exert strong membrane destabilization selectively in acidic endosomal compartments for efficient endosomal escape with low cytotoxicity [19–22]. Note that PAsp(DET) possesses two unique advantages for its excellent transfection: 1) the pH-selective membrane destabilization based on the distinctive two step protonation behavior in the side chain, i.e., mono-protonated form with minimal membrane damages at neutral pH and di-protonated form exerting strong membrane disruption at acidic pH [20]; 2) the spontaneous biodegradability based on the selective backbone cleavage even under physiological conditions [21].

In this work, in order to improve the endosomal escape as well as the colloidal stability of CaP precipitates, a block copolymer of PEG and an endosomal escaping polymer was synthesized and integrated into the CaP nanoparticles incorporating siRNA. Indeed, we modified the flanking primary amines of PEG-PAsp(DET) with *cis*-aconitic anhydride [23,24] to convert the cationic charges to net negative ones with two carboxylates of the *cis*-aconityl moiety (PEG-poly{*N*-[*N*′-(*N*″-*cis*-aconityl-2-aminoethyl)-2-aminoethyl]aspartamide}, PEG-PAsp(DET-Aco)) for effective binding to CaP nanoparticles. Noteworthy, the prepared *cis*-aconitylamide shows high stability at neutral and basic pHs but it becomes cleavable at acidic pH to reproduce cationic PAsp(DET) from anionic PAsp(DET-Aco) in endosome/lysosome, which is termed the charge-conversional polymer [23–25]. The hybrid nanoparticle prepared from PEG-PAsp(DET-Aco), siRNA, and CaP does not contain inherent toxic materials, such as polycations, thereby leading to potentially lower toxicity compared to conventional polyplex carriers from polycations and siRNA. Thus, the nanoparticles prepared by simple mixing of each component were physicochemically and biologically characterized by the comparison with non-charge-conversional control polyanions to demonstrate the utility of our hybrid system from the PEG–charge-conversional polymer for siRNA delivery.

2. Material and methods

2.1. Materials

cis-Aconitic anhydride, tricarballylic acid, and Dulbecco's modified eagle's medium (DMEM) were purchased from Sigma–Aldrich (St. Louis, MO). α-Methoxy-ω-amino-poly(ethylene glycol) (MeO–PEG–NH_2) (M_w: 12,000) and β-benzyl-L-aspartate *N*-carboxyanhydride (BLA–NCA) were obtained from NOF Co, Inc. (Tokyo, Japan) and Chuo Kaseihin Co., Inc. (Tokyo, Japan), respectively. *N*-Methyl-2-pyrrolidone (NMP), diethylenetriamine (DET), dimethyl sulfoxide (DMSO), *N*,*N*-dimethylformamide (DMF), dichloromethane (DCM), and acetic anhydride were purchased from Tokyo Chemical Industry Co. Ltd. (Tokyo, Japan) or Nacalai Tesque (Tokyo, Japan), and used after a conventional distillation. Acetic acid, acetonitrile, acetone, diethyl ether, and hydrochloric acid were purchased from Wako Pure Chemical Industries Ltd. (Osaka, Japan). Fetal bovine serum (FBS) was purchased from Dainippon Sumitomo Pharma Co., Ltd. (Osaka, Japan). The primers for human actin and human VEGF were synthesized by Hokkaido System Science (Hokkaido, Japan) and the sequences are: CCAACCGCGAGAAGATGA (actin forward); CCAGAGGCGTACAGGGATAG (actin reverse); AGTGGTCCCAGGCTGCAC (VEGF forward); TCCATGAACTTCACCACTTCGT (VEGF reverse). All the siRNAs were synthesized by Hokkaido System Science (Hokkaido, Japan) and the sequences of VEGF siRNA (siVEGF) are: 5′-GGAGUACCCUGAUGAGAUCdTdT-3′ (sense); 5′-GAUCUCAUCAGGGUACUCCdTdT-3′ (antisense), and GL3 luciferase siRNA (siGL3) are: 5′-CUU ACG CUG AGU ACU UCG AdTdT-3′ (sense); 5′-UCG AAG UAC UCA GCG UAA GdTdT-3′ (antisense).

2.2. Synthesis of block copolymer with poly(ethylene glycol) and charge-conversional polymer (PEG–CCP) segments

2.2.1. Synthesis of poly(ethylene glycol)-b-poly{N-[N-(2-aminoethyl)-2-aminoethyl] aspartamide} (PEG-PAsp(DET))

PEG-PAsp(DET) was prepared as previously reported with slight modification [21]. Briefly, BLA–NCA (780 mg; 3.13 mmol) was dissolved in 0.7 mL of DMF, and then in 7.3 mL of DCM. The polymerization was initiated from the primary amino group of MeO–PEG–NH_2 ($M_w = 12{,}000$, 500 mg; 0.0417 mmol) to obtain PEG–PBLA (1100 mg) as a precursor. Size exclusion chromatography (SEC) was performed to determine the molecular weight distribution (M_w/M_n) of the obtained PEG–PBLA using a TOSOH HLC-8220 equipped with TSK gel columns (SuperAW4000 and SuperAW3000 × 2; eluent: NMP with 50 mM LiBr; flow rate: 0.3 mL min^{-1}; temperature: 40 °C) and an internal refractive index (RI) detector. The M_w/M_n was confirmed to be 1.07 from the SEC chart using PEG standards for the M_w calibration (data not shown). The degree of polymerization of PBLA in PEG–PBLA was determined to be 96 from the peak intensity ratio of the methylene protons of PEG ($-OCH_2CH_2-$, $\delta = 3.5$ ppm) to the benzyl protons of PBLA ($C_6H_5CH_2-$, $\delta = 5.1$ and 7.3 ppm) in the ^1H NMR measurement (data not shown). All of the NMR assays were performed using (3-(trimethylsilyl)-3,3,2,2-tetradeuteropropionic acid sodium salt d_4-TSPA) as an internal standard. Then, PEG–PBLA (100 mg) was dissolved in NMP (2 mL) and cooled at 5 °C. Diethylenetriamine (DET) (3 mL; 100 equiv to benzyl groups of PBLA segment) was diluted with the same volume of NMP, and then the first solution was added and stirred for 4 h at 0 °C (ice bath). The reaction was stopped adding the polymer solution to cold 20% acetic acid (30 mL) drop-by-drop. The neutralized solution was dialyzed against 0.01 M hydrochloric acid solution and then in de-ionized water at 4 °C. As a hydrochloride salt form, a white powder was obtained after lyophilization of the dialyzed solution (91.2 mg, 69.6% yield). The quantitative conversion of the BLA to Asp(DET) was confirmed from the peak intensity ratio of the methylene protons in PEG ($-OCH_2CH_2-$, $\delta = 3.7$ ppm) to the ethylene protons in the 1,2-diaminoethane moiety ($H_2N(CH_2)_2NH(CH_2)_2NH-$, $\delta = 2.8-3.4$ ppm) in the ^1H NMR spectrum in D_2O at 50 °C (Supporting Information).

2.2.2. Synthesis of poly(ethylene glycol)-b-poly{N-[N′-(N″-cis-aconityl-2-aminoethyl)-2-aminoethyl]aspartamide} (PEG-PAsp(DET-Aco))

PEG-PAsp(DET) (17.5 mg, 0.0538 mmol of primary amine) was dissolved in 0.5 M $NaHCO_3$ at pH 9.1 (50 mL). *cis*-Aconitic anhydride powder (420 mg, 2.69 mmol) was added to the solution slowly and stirred at 0 °C for 2 h. The reaction mixture was purified by centrifugal ultrafiltration with Amicon Ultra (MWCO = 10,000; Millipore (Billerica, MA)) three times with de-ionized water at 4 °C. The final product was obtained as a white powder after lyophilization (14.9 mg, 64.7% yield). The quantitative conversion of primary amines in Asp(DET) side chain to *cis*-aconitylamide was confirmed from the peak intensity ratio of the methine protons in the main chain ($-COCH_2CH(CO-)NH-$, $-COCH(CH_2-)NH-$, $\delta = 4.8$ ppm) to methine protons of the *cis*-aconityl moiety ($-COCH{:}C(COONa)CH_2COONa$, $\delta = 6.0$ ppm) in ^1H NMR spectrum in D_2O at 50 °C (Fig. 1).

2.3. Synthesis of block copolymer with poly(ethylene glycol) and non-charge-conversional polymers (PEG–nCCP) segments

2.3.1. Synthesis of carballylic anhydride

Carballylic anhydride was prepared as previously reported [26] with slight modification. Briefly, tricarballylic acid (4.4 g, 0.025 mol) was reacted with acetic anhydride (4.73 mL, 0.05 mol) at 45 °C for 1 h. The excess of acetic anhydride was evaporated under reduced pressure. Further, the product was dissolved in the minimum amount of ethyl acetate at 80 °C and filtered. The solution was allowed to stand for 5 h at room temperature and then overnight at 4 °C. The obtained crystal was then vacuum-filtered, washed with excess of diethyl ether, and then dried in vacuum to yield a white crystal (760 mg, 19.2% yield). The reaction was confirmed by ^1H NMR spectrum in acetone at 25 °C ($-COCH_2CH(CH_2COOH)CO-$, $\delta = 2.94$, 2.86 ppm), (CH_2COOH, $\delta = 2.44$ ppm) (data not shown).

2.3.2. Synthesis of poly(ethylene glycol)-b-poly{N-[N′-(N″-carballylyl-2-aminoethyl)-2-aminoethyl]aspartamide} (PEG-PAsp(DET-Car))

PEG-PAsp(DET) (15 mg, 0.046 mmol of primary amine) was dissolved in 0.5 M $NaHCO_3$ at pH 9.1 (50 mL). Carballylic anhydride powder (Car) (363 mg, 2.3 mmol) was added to the solution slowly and stirred at 0 °C for 2 h. The reaction mixture was purified by centrifugal ultrafiltration with Amicon Ultra (MWCO = 10,000; Millipore (Billerica, MA)) three times with de-ionized water at 4 °C. The final product was obtained as a white powder after lyophilization (13.5 mg, 68.3% yield). The quantitative conversion of the primary amines in the Asp(DET) side chain to carballylylamide was confirmed from the peak intensity ratio of the methine protons in the main chain ($-COCH_2CH(CO-)NH-$, $-COCH(CH_2-)NH-$, $\delta = 4.8$ ppm) to the methylene protons of the carballylyl moiety ($-CH_2CH(COONa)CH_2COONa$, $\delta = 2.5$) in the ^1H NMR spectrum in D_2O at 50 °C (Supporting Information).

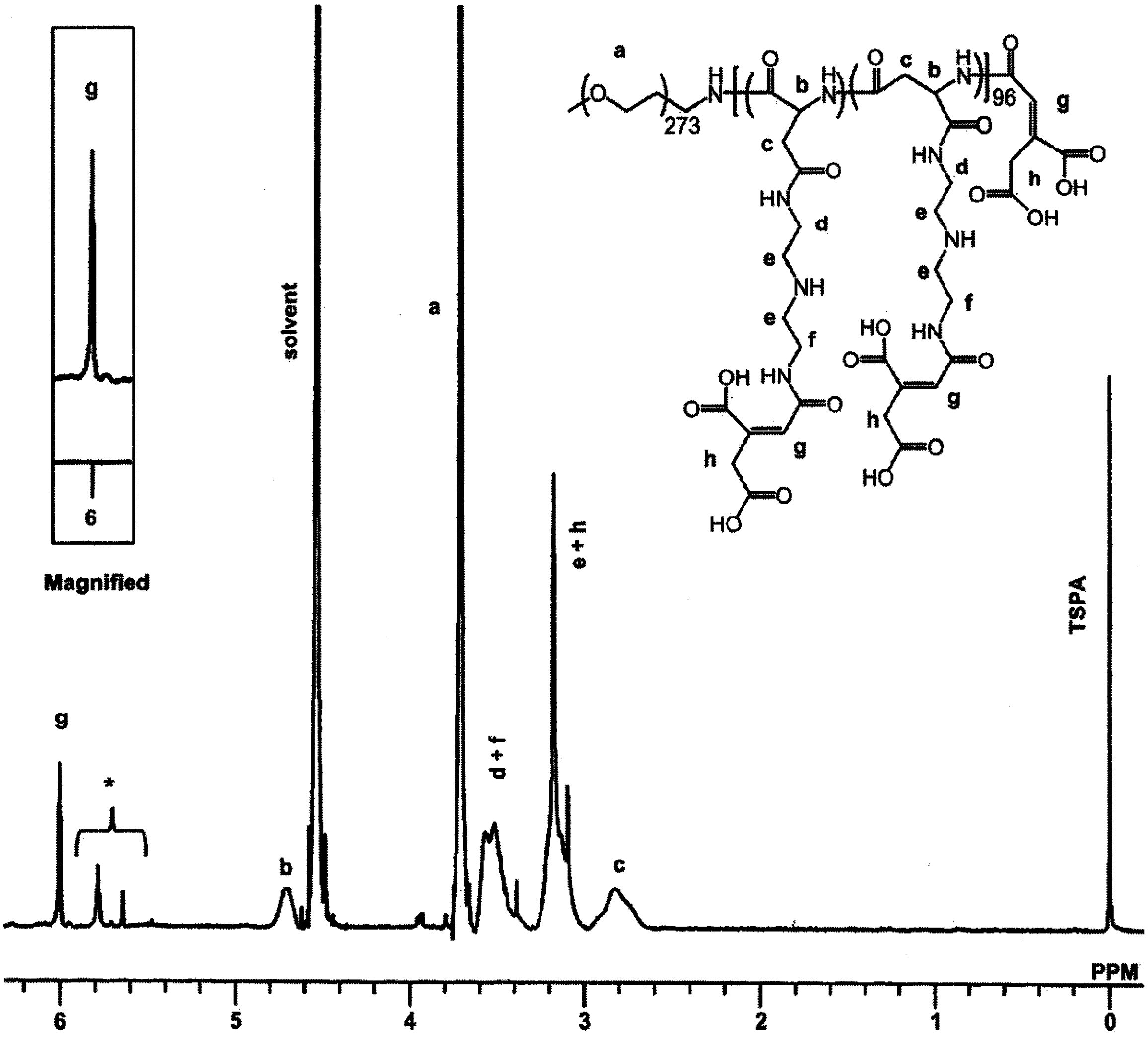

Fig. 1. ^1H NMR spectrum of the synthesized PEG-polyanion block copolymer, PEG-PAsp(DET-Aco) (Concentration: 10 mg/mL, Solvent: D_2O, Temperature: 50 °C). *Decarboxilated itaconitylamide (Supporting Information).

2.3.3. Synthesis of poly(ethylene glycol)-b-poly(aspartic acid) (PEG-PAsp)

PEG–PBLA (20 mg, 0.06 mmol) was dissolved in acetonitrile (1.5 mL). Aqueous sodium hydroxide (0.5 N, 6 mL, 50 equiv to benzyl group of PBLA segment) was added to the first solution and allowed to react for 1 h stirring at room temperature. The solution was dialyzed against de-ionized water. A white powder was obtained after lyophilization of the dialyzed solution (18.2 mg, 93.0% yield). The complete deprotection of the flanking benzyl esters in PBLA was confirmed by the peak disappearance of benzyl protons of PBLA ($-CH_2C_6H_5$, $\delta = 7.3$) in the ^1H NMR spectrum in D_2O at 50 °C (data not shown).

2.4. Preparation of PEG-polyanion/siRNA/CaP hybrid nanoparticles

A solution of 2.5 M $CaCl_2$ was diluted in 10 mM Tris/HCl buffer (pH 7.5) (1 μL: 11.5 μL). Another solution containing PEG-PAsp(DET-Aco) or PEG-PAsp(DET-Car) (1000 μg/mL) in 10 mM Tris/HCl buffer (pH 7.5) was mixed with a solution of 15 μM siRNA in 10 mM Hepes buffer (pH 7.2) and with 50 mM Hepes buffer containing 1.5 mM Na_3PO_4 and 140 mM NaCl (pH 7.5) (2.5 μL: 5 μL: 5 μL). The former solution was mixed with the latter solution by pipetting for around 20 s (final siRNA concentration; 3 μM). A control nanoparticle containing PEG-PAsp was built as previously described [9]. Each sample solution was used immediately after preparation.

2.5. Dynamic light scattering (DLS)

For the determination of size distribution of hybrid nanoparticles, DLS measurements were carried out at 25 °C using a Zetasizer Nano ZS (Malvern Instruments, UK) at a detection angle of 173° with a He–Ne laser (633 nm) as the incident beam. The data obtained from the rate of decay in the photon correlation function were analyzed with a cumulant method to obtain the corresponding hydrodynamic diameters and polydispersity indices (PdI) (μ/Γ^2) of the nanoparticles.

2.6. Determination of siRNA encapsulated in hybrid nanoparticle

The assay to estimate the amount of siRNA encapsulated in hybrid nanoparticles was carried out as previously reported [11]. Briefly, the sample solutions were centrifuged at 15,000g for 30 min to precipitate the nanoparticles. The supernatant was carefully collected to determine the siRNA concentration by measurement of absorbance at 260 nm (Abs_{260}). The percentage of the loaded siRNA was calculated as follows;

Encapsulated percentage (%) = 100 – (Abs_{260} after centrifuge)/(Abs_{260} before centrifuge) × 100

2.7. Transmission electron microscopy (TEM) observation

TEM observation was conducted using H-7000 electron microscope (Hitachi, Tokyo, Japan) operated at 75 kV acceleration voltages. Copper TEM grids with carbon-coated collodion film were glow-discharged for 20 s using an Eiko IB-3 ion coater (Eiko Engineering Co. Ltd., Japan). The grids were dipped into complex solution with 3 μM siRNA, which was mixed with uranyl acetate solution (2% (w/v)), for 30 s. After excess solution was removed using a filter paper, the sample grids were allowed to dry in air and then TEM observation was carried out.

2.8. Cell viability assay

For the cytotoxicity assay, PanC-1 cells (Pancreatic cancer cells, ATCC Number: CRL-1469) were seeded with 100 μL of DMEM containing 10% FBS in a 96 well plate (5000 cells/well) and incubated for 24 h. The nanoparticles (containing 10–1500 nM siRNA) were added with the fresh medium containing 10% FBS, and the cell viability was evaluated after 48-h incubation by Cell Counting Kit-8 (Dojindo, Kumamoto, Japan) according to the protocol provided by the manufacturer. Each well was measured by reading the absorbance at 450 nm in a Microplate Reader (Bio-Rad Model 680, Bio-Rad Laboratories, UK). The results were expressed as the percentage (%) of the control cells, which were incubated only with the culture medium.

2.9. Confocal laser scanning microscopy (CLSM) observation

PanC-1 cells were cultured with 1.5 mL of DMEM containing 10% FBS on 35-mm glass-base dishes (Iwaki, Japan) at 5×10^4 cells/dish. After 24 h, the medium was exchanged with fresh one and Cy5-labeled siRNA-containing nanoparticles were applied to the dish (100 nM siRNA). The nuclei and the endosome/lysosome were stained with Hoechst 33342 (Dojindo Laboratories, Kumamoto, Japan) for 5 min and LysoTracker Green (Molecular Probes, Eugene, OR) for 15 min before CLSM imaging, respectively. Cells were rinsed 3 times with PBS and fresh medium was added prior to the imaging. CLSM images were acquired at 3 and 24 h after nanoparticle administration, using a Zeiss LSM 510 META (Carl Zeiss, Germany) with a water-immersion 63× objective (C-Apochromat, Carl Zeiss). Excitation wavelengths were 488 nm (argon laser), 633 nm (He–Ne laser), and 710 nm (Mai Tai laser, operated in a two-photon mode) for LysoTracker, Cy5, and Hoechst 33342, respectively. The co-localization ratio was calculated as previously described [24] with the formula:

Co-localization ratio = number of yellow pixels/number of yellow and red pixels.

2.10. Real-time reverse transcription (RT)-PCR

PanC-1 cells were seeded with 2000 μL of DMEM containing 10% FBS on a 6 well plate at 8×10^4 cells/well. After 24 h, nanoparticles were added with fresh medium (60 nM siRNA). After 3 h of exposing the cells to nanoparticles, the medium was changed to fresh one. Twenty four hours later, cells were harvested and RNA was extracted using the RNeasy Mini Kit (Qiagen, Valencia, CA), according to the manufacturer's instruction. The amount of extracted RNA was measured and standardized after the genomic DNA elimination for the cDNA synthesis (QuantiTect Reverse Transcription, Quiagen, Valencia, CA). Real-time RT-PCR was performed using the ABI 7500 Fast Real-time RT-PCR System (Applied Biosystems, Foster City, CA) and QuantiTect SYBR Green PCR Master Mix (Qiagen, Valencia, CA). The actin was used as a house-keeper gene and the obtained data were normalized before statistical analysis.

2.11. Statistical analysis

The analysis of variance (ANOVA) was performed to test the treatment effects, and Bonferroni's test was used as *post hoc* pairwise comparisons between individual treatment groups, using the software GraphPad Prisma 3.0 (GraphPad Software, Inc.). Statistical significance is represented as * for $p < 0.05$ and ** for $p < 0.01$. Unless indicated, all experiments were performed in triplicate ($N = 3$) and the results reported were expressed as mean values (±SEM).

3. Results and discussion

3.1. Synthesis of charge-conversional and non-charge-conversional polymers

The synthesis route of PEG-PAsp(DET-Aco) as a charge-conversional polyanion is illustrated in Scheme 1, as well as two polyanions used as controls without the charge-conversional property. PEG-PAsp(DET) was synthesized from PEG–PBLA (M_w of PEG 12,000; DP of PBLA 96) by aminolysis reaction with excess of DET molecules. The ^1H NMR measurement revealed the quantitative introduction of the *N*-(2-aminoethyl)-2-aminoethyl moiety for successful synthesis of PEG-PAsp(DET) (data not shown). Further, the *cis*-aconityl moiety (Aco) was introduced into the primary amine in the side chain of PAsp(DET) by reacting *cis*-aconitic anhydride with PEG-PAsp(DET) to form an acid-labile *cis*-aconitylamide in the side chain. The quantitative conversion of primary

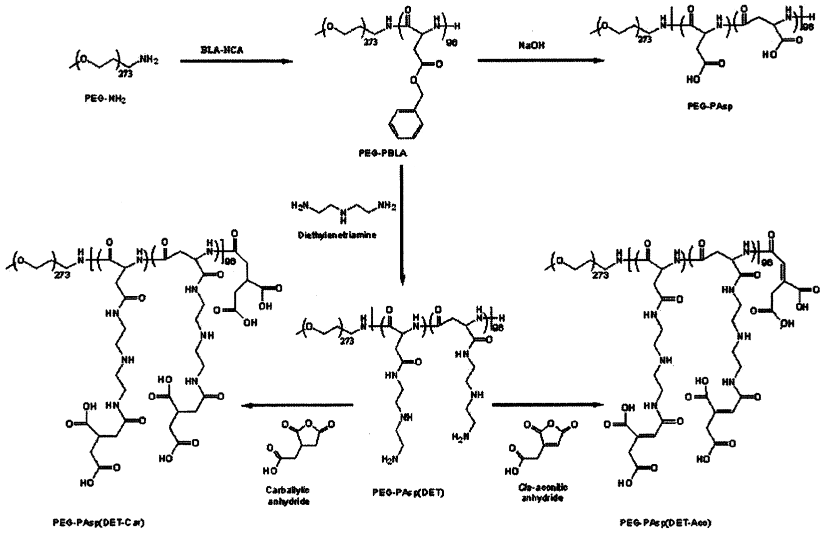

Scheme 1. Synthetic routes of PEG-PAsp(DET-Aco), PEG-PAsp(DET-Car), and PEG-PAsp.

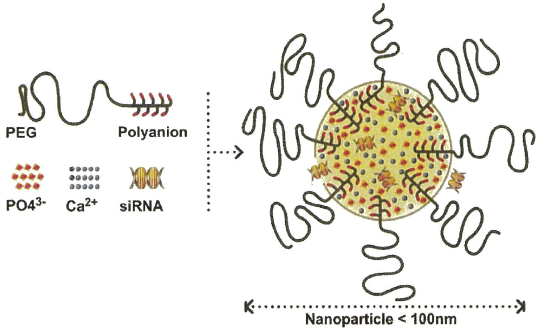

Fig. 2. Schematic illustration of PEG-polyanion/siRNA/CaP hybrid nanoparticles.

amines in Asp(DET) side chain to *cis*-aconitylamide was confirmed from the peak intensity ratio of the methine protons in the main chain to methine protons of the *cis*-aconityl moiety in the ^1H NMR spectrum in D_2O (Fig. 1). Although it was also possible to observe the formation of reaction subproducts [27], the desired product of PEG-PAsp(DET-Aco) was obtained in a high ratio (80%). PEG-PAsp (DET-Car) without the acid-labile bond as a control was synthesized by reacting PEG-PAsp(DET) with carballylic anhydride similarly. The quantitative conversion of the primary amines in the Asp(DET) side chain to carballylylamide was confirmed from the peak intensity ratio of the methine protons in the main chain to the methine and methylene protons of carballylyl moiety in the ^1H NMR spectrum in D_2O (Supporting Information). In addition, another control polyanion, PEG-PAsp, was prepared by the deprotection of benzyl ester group from PEG–PBLA. The successful deprotection of benzyl ester group was confirmed from the corresponding peak disappearance in the ^1H NMR spectrum in D_2O (data not shown). Note that all the reactions were confirmed to proceed without the spontaneous main-chain cleavage [21] from aqueous GPC charts of obtained polymers (data not shown).

3.2. PEG-polyanion/siRNA/CaP hybrid nanoparticle formation and characterization

Great advantages in the utilization of CaP precipitates as a transfection reagent are the fact that they are prepared by a simple and inexpensive method, and also that it efficiently binds/encapsulates polyanions/nucleic acids during the formation process [28,29]. Through self-assembly, CaP nanoparticles containing nucleic acid are formed by the precipitation method in which calcium chloride and phosphate solutions are mixed in the presence of siRNA. However, simple CaP precipitates have potential problems to overcome for efficient nucleic acids delivery; one is the increase in size with time to form large agglomerates in aqueous solutions, and another is poor endosomal escape. To prevent the size increase in CaP precipitates, our previous studies have addressed a preparation of PEG-coated CaP hybrid nanoparticles by mixing of PEG-polyanion block copolymers [9,11–14]. In this study, for further improvement of the PEG-coated CaP nanoparticles, we focused on endosomal escape of the nanoparticles to enhance the gene knockdown efficiency, thus applying a charge-conversional structure PAsp(DET-Aco) [23,24] for the polyanionic segment. Indeed, the hybrid nanoparticles were prepared from the inorganic CaP core, siRNA as a therapeutic payload, and the PEG-PAsp(DET-Aco) as a charge-conversional unit for endosomal escape with minimal cytotoxicity, by mixing calcium and phosphate ionic solutions containing siRNA and the charge-conversional polymer as illustrated in Fig. 2.

The TEM observations with uranyl acetate as a staining agent (Fig. 3A) revealed hybrid nanoparticles with relatively homogenous spherical shape and average size of 42 ± 5 nm. Furthermore, the DLS measurements provided a size histogram in number statistics showing a narrow unimodal distribution with the peak at 38 nm

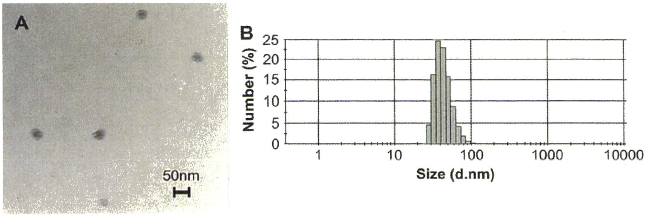

Fig. 3. Size and morphology of PEG-PAsp(DET-Aco)/siRNA/CaP hybrid nanoparticles. A: TEM image (Scale Bar: 50 nm). B: Histogram in number statistics determined by DLS measurement (1 mg/mL PEG-PAsp(DET-Aco) and 3 μM siRNA).

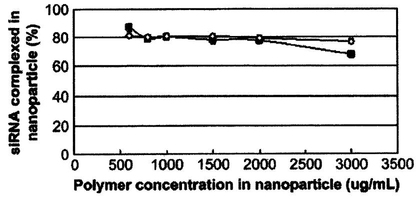

Fig. 4. Percentage of siRNA loaded by the hybrid nanoparticle at varying polymer concentrations (3 μM siRNA). Closed square: PEG-PAsp(DET-Aco), Open diamond: PEG-PAsp(DET-Car).

(Fig. 3B), which was well correlated to the size determined by the TEM observations (Fig. 3A). Samples were confirmed to have the same size even after prolonged incubation time. These results indicate that hybrid nanoparticles can be obtained in a controllable manner using the charge-conversional polymer as colloidal stability agent.

The amount of siRNA encapsulated in the hybrid nanoparticles was monitored against polyanion concentration, determined by the centrifugal assay as previously reported [11]. Effective encapsulation of siRNA in the nanoparticles (around 80%) was confirmed in PEG-PAsp(DET-Aco) concentration between 600 and 2000 μg/mL, while a slight decrease was observed at the concentration of 3000 μg/mL (around 70%) (Fig. 4). Note that the similar binding tendency was observed for the nanoparticle from PEG-PAsp(DET-Car). The siRNA-loading capacities obtained here were close to those found in our previous work with PEG-PAsp (around 85%) [11], indicating efficient entrapment of siRNA by this method regardless of polyanion structures.

3.3. Gene knockdown and cell viability assays

The development of an effective and non-cytotoxic carrier is the main challenge to the success in RNAi therapy. We verified the gene knockdown efficiency of the hybrid nanoparticles to a cultured pancreatic cancer cell (PanC-1) by measuring the level of mRNA. Here, vascular endothelial growth factor (VEGF) was chosen as a target gene because many cancer cells up-regulate VEGF expression to promote angiogenesis, a process characterized by the formation of new blood vessels from a pre-existing vascular network [30,31], facilitating the tumor growth and proliferation. Hence, VEGF knockdown in such cancer cells with siRNA *in vivo* is expected to be a promising strategy to suppress the tumor growth and control cancer evolution (anti-angiogenic therapy).

Hybrid nanoparticles containing 60 nM siVEGF or siLuc as a non-targeted control sequence were applied to PanC-1 cells, and after 3 h of exposure time the medium was replaced and cells were further incubated for 24 h. Thereafter, the real-time RT-PCR analysis was used to determine the mRNA for VEGF. The results revealed that all the tested hybrid nanoparticles with siVEGF possessed potential gene knockdown activity, whereas the nanoparticles with siLuc and naked siVEGF showed no gene knockdown (Fig. 5), indicating the siVEGF sequence-specific gene knockdown with the hybrid nanoparticles. Among them, the nanoparticle from PEG-PAsp(DET-Aco) presented the only significant and highest gene knockdown (~82%). The comparison of PEG-PAsp(DET-Aco) with the other PEG-polyanions strongly suggests that the acid-labile *cis*-aconitylamide in PEG-PAsp(DET-Aco) should be essential for the significant gene knockdown. Next, the cytotoxicity of the hybrid nanoparticles was evaluated to PanC-1 cells. A wide range of siRNA concentration was tested from 10 to 1500 nM along with the increase in all the other components. As shown in Fig. 6, no significant cytotoxicity was observed for both hybrid nanoparticles from PEG-PAsp(DET-Aco/Car) even at the highest concentration (50 μg/mL PEG-polyanion, 1.5 μM siRNA). From these results, we concluded that the hybrid nanoparticles from PEG-PAsp(DET-Aco) allowed efficient siRNA delivery into the cytoplasm of cultured PanC-1 with negligible cytotoxicity.

3.4. Cellular uptake and intracellular trafficking

In siRNA transfection process, after cellular internalization as the first hurdle, siRNA carriers will be delivered to early endosomes,

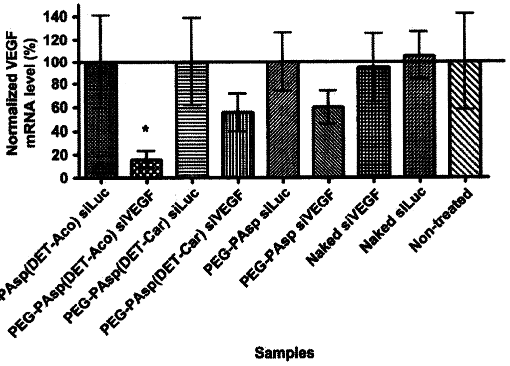

Fig. 5. Gene knockdown in PanC-1 at 24 h after 3 h of nanoparticles exposition to cells (60 nM siRNA, $N = 9$). Controls were set as 100%. $^*p < 0.05$ comparing to controls (ANOVA followed by Bonferroni).

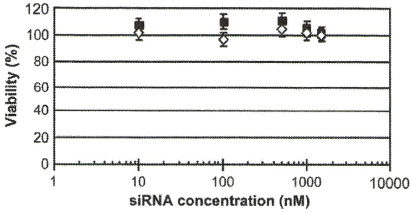

Fig. 6. Cell viability of PanC-1 cells incubated with hybrid nanoparticles for 48 h ($N = 6$). siLuc concentration was changed from 10 to 1500 nM, corresponding to the polymer concentration from 0.7 to 50 μg/mL. Closed square: PEG-PAsp(DET-Aco), Open diamond: PEG-PAsp(DET-Car).

followed by the movement to late endosomes/lysosomes for siRNA degradation [6]. Thus, the smooth endosomal escape is a critical requirement for the effective gene silencing with siRNA. In the preceding section, the utility of PEG-PAsp(DET-Aco) was demonstrated for significant VEGF mRNA knockdown without marked cytotoxicity. Here, we verified whether the excellent gene knockdown is attributed to endosomal escape with PEG-PAsp(DET-Aco) along with our initial hypothesis. Accordingly, we observed the intracellular trafficking of each hybrid nanoparticle after 3- and 24-h incubation with PanC-1 cells. In the obtained images, Cy5-siRNA, endosomes/lysosomes, and nuclei were shown in red, green, and blue, respectively, and thus yellow pixels result in the merge of red and green pixels, indicating the co-localization of Cy5-siRNA with endosome/lysosome. The images of PanC-1 cells treated with PEG-PAsp(DET-Aco)/PEG-PAsp(DET-Car) nanoparticles displayed red and/or yellow regions with 3-h incubation (Fig. 7A and B), indicating that both of the nanoparticles allowed the significant cellular uptake of Cy5-siRNA. In these two images, only the nanoparticles containing PEG-PAsp(DET-Aco) in the formulation presented widely extended red regions in cells (Fig. 7A), corresponding to the presence of Cy5-siRNA in the cytoplasm. In contrast, the cells treated with the other nanoparticles containing PEG-PAsp(DET-Car) mainly displayed perinuclear yellow spots (Fig. 7B), indicating the endosomal/lysosomal capture of Cy5-siRNA. These results are well consistent with our hypothesis that the integration of PEG-PAsp(DET-Aco) into the nanoparticles intensely facilitates the endosomal escape of the hybrid nanoparticles in the early stage of transfection, presumably due to the charge-conversional property

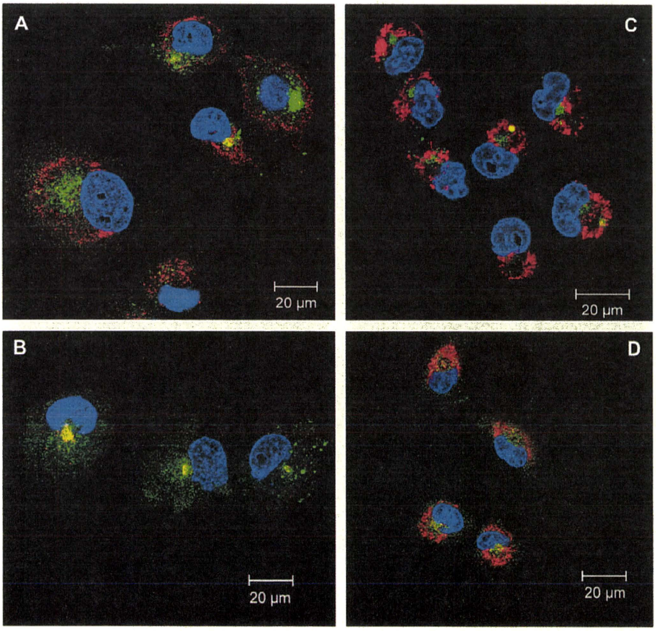

Fig. 7. Confocal laser scanning microscopic observation for intracellular trafficking of hybrid nanoparticles. Images were taken at 3 and 24 h after nanoparticle application. A: PEG-PAsp(DET-Aco), B: PEG-PAsp(DET-Car) nanoparticles incubated for 3 h (100 nM siRNA). C: PEG-PAsp(DET-Aco), D: PEG-PAsp(DET-Car) nanoparticles incubated for 24 h (100 nM siRNA). Blue: Hoechst at 710 nm (two-photon excitation); Green: Lysotracker at 488 nm; and Red: Cy5 at 633 nm.

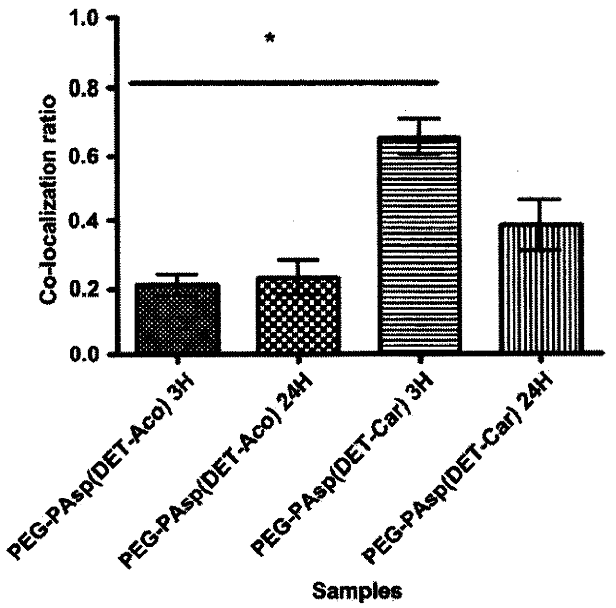

Fig. 8. Co-localization ratio of Cy5-labeled siRNA with endosome/lysosome obtained by analyzing the images. Results were expressed as mean ± SEM (from three cells) (*$p < 0.01$).

to reproduce the endosomal membrane destabilizing polycation, PAsp(DET), in the acidic endocytic vesicles. On the other hand, after 24-h incubation, the cells treated with PEG-PAsp(DET-Car) nanoparticles obviously increased red regions (Fig. 7D), suggesting that the hybrid nanoparticles might originally have an endosomal escaping ability apart from the charge-conversional polymers. A possible explanation of this delayed endosomal escape is that CaP core disassembles under a low ionic condition in endocytic vesicles for increased-ion induced-osmotic pressure to induce endosomal membrane disruption [11], similar to the proton sponge hypothesis known to polyethyleneimine [32]. Eventually, the co-localization of Cy5-siRNA with endosome/lysosome was quantitatively analyzed for PEG-PAsp(DET-Aco) and PEG-PAsp(DET-Car), as summarized in Fig. 8. The obtained tendency in endosomal escape of each nanoparticle is well correlated with the result in the gene knockdown experiment (Fig. 5). Earlier endosomal escape of siRNA by PEG-PAsp (DET-Aco) probably leads to more efficient gene knockdown with the nanoparticles.

4. Conclusion

This work was aimed to develop a hybrid nanocarrier system consisting of CaP and the PEG–charge-conversional polymer for safe and efficient siRNA delivery. To improve the endosomal escape of the nanoparticles, we integrated the charge-conversional polymer PEG-PAsp(DET-Aco) into the nanoparticles, in which PEG-PAsp (DET-Aco) induces the destabilization of endosomal membrane by producing a polycation PAsp(DET) via the selective cleavage of *cis*-aconitylamide in acidic endosome/lysosome. The size less than 100 nm with narrow size distribution and a high siRNA-loading capacity were confirmed for PEG-PAsp(DET-Aco)/siRNA/CaP nanoparticles, which achieved strong VEGF knockdown to PanC-1 with negligible cytotoxicity through the rapid endosomal escape. These findings demonstrate our hybrid system as a promising candidate to future *in vivo* siRNA applications for pancreatic cancer treatment based on anti-angiogenic therapy.

Acknowledgments

This research is supported by the Japan Society for the Promotion of Science (JSPS) through its "Funding Program for World-Leading Innovative R&D on Science and Technology (FIRST Program)". F.P. acknowledges the fellowship from Ministry of Education, Science, Sports and Culture, Japan (MEXT).

Appendix

Figures with essential color discrimination. Figs. 2, 3 and 7 in this article are difficult to interpret in black and white. The full color images can be found in the online version, at doi:10.1016/j.biomaterials.2010.12.057.

Appendix. Supporting information

Supplementary data associated with this article can be found, in the online version, at doi:10.1016/j.biomaterials.2010.12.057.

References

[1] Fire A, Xu S, Montgomery MK, Kostas SA, Driver SE, Mello CC. Potent and specific genetic interference by double-stranded RNA in *Caenorhabditis elegans*. Nature 1998;391:806–11.
[2] Elbashir SM, Harborth J, Lendeckel W, Yalcin A, Weber K, Tuschl T. Duplexes of 21-nucleotide RNAs mediate RNA interference in cultured mammalian cells. Nature 2001;411:494–8.
[3] International Human Genome Sequencing Consortium. Initial sequencing and analysis of the human genome. Nature 2001;409:860–921.
[4] Venter JC, Adams MD, Myers EW, Li PW, Mural RJ, Sutton GG, et al. The sequence of the human genome. Science 2001;291:1304–51.
[5] International Human Genome Sequencing Consortium. Finishing the euchromatic sequence of the human genome. Nature 2004;431:931–45.
[6] Whitehead KA, Langer R, Anderson DG. Knocking down barriers: advances in siRNA delivery. Nat Rev Drug Discov 2009;8(2):129–38.
[7] Graham FL, van der Eb AJ. A new technique for the assay of infectivity of human adenovirus 5 DNA. Virology 1973;52:456–67.
[8] Jordan M, Schallhorn A, Wurm FM. Transfecting mammalian cells: optimization of critical parameters affecting calcium–phosphate precipitate formation. Nucleic Acids Res 1996;24:596–601.
[9] Kakizawa Y, Kataoka K. Block copolymer self-assembly into monodispersive nanoparticles with hybrid core of antisense DNA and calcium phosphate. Langmuir 2002;18:4539–43.
[10] Maitra A. Calcium phosphate nanoparticles: second-generation nonviral vectors in gene therapy. Expert Rev Mol Diagn 2005;5(6):893–905.
[11] Kakizawa Y, Furukawa S, Kataoka K. Block copolymer-coated calcium phosphate nanoparticles sensing intracellular environment for oligodeoxynucleotide and siRNA delivery. J Control Release 2004;97:345–56.
[12] Kakizawa Y, Miyata K, Furukawa S, Kataoka K. Size-controlled formation of a calcium phosphate-based organic-inorganic hybrid vector for gene delivery using poly(ethylene glycol)-*block*-poly(aspartic acid). Adv Mater 2004;16 (8):699–702.
[13] Kakizawa Y, Furukawa S, Ishii A, Kataoka K. Organic–inorganic hybrid-nanocarrier of siRNA constructing through the self-assembly of calcium phosphate and PEG-based block aniomer. J Control Release 2006;111:368–70.
[14] Zhang MZ, Ishii A, Nishiyama N, Matsumoto S, Ishii T, Yamasaki Y, et al. PEGylated calcium phosphate nanocomposites as smart environment-sensitive carriers for siRNA delivery. Adv Mater 2009;21(34):3520–5.
[15] Francis G, Delgado C, Fisher D, Malik F, Agrawal AK. Polyethylene glycol modification: relevance to improved methodology to tumour targeting. J Drug Target 1996;3:321–40.
[16] Monfardini C, Veronese FM. Stabilization of substances in the circulation. Bioconjug Chem 1998;9:418–50.
[17] Kataoka K, Harada A, Nagasaki Y. Block copolymer micelles for drug delivery: design, characterization and biological significance. Adv Drug Deliv Rev 2001;47:113–31.
[18] Dominska M, Dykxhoorn DM. Breaking down the barriers: siRNA delivery and endosome escape. J Cell Sci 2010;123:1183–9.
[19] Kanayama N, Fukushima S, Nishiyama N, Itaka K, Jang W-D, Miyata K, et al. A PEG-based biocompatible block catiomer with high buffering capacity for the construction of polyplex micelles showing efficient gene transfer toward primary cells. ChemMedChem 2006;1:439–44.
[20] Miyata K, Oba M, Nakanishi M, Fukushima S, Yamasaki Y, Koyama H, et al. Polyplexes from poly(aspartamide) bearing 1,2-diaminoethane side chains induce pH-selective, endosomal membrane destabilization with amplified transfection and negligible cytotoxicity. J Am Chem Soc 2008;130(48): 16287–94.

[21] Itaka K, Ishii T, Hasegawa Y, Kataoka K. Biodegradable polyamino acid-based polycations as safe and effective gene carrier minimizing cumulative toxicity. Biomaterials 2010;31(13):3707–14.

[22] Kim HJ, Ishii A, Miyata K, Lee Y, Wu S, Oba M, et al. Introduction of stearoyl moieties into a biocompatible cationic polyaspartamide derivative, PAsp (DET), with endosomal escaping function for enhanced siRNA-mediated gene knockdown. J Control Release 2010;145(2):141–8.

[23] Lee Y, Miyata K, Oba M, Ishii T, Fukushima S, Han M, et al. Charge conversion ternary polyplex with endosomes disruption moiety: a technique for efficient and safe gene delivery. Angew Chem Int Ed Engl 2008;120:5241–4.

[24] Sanjoh M, Hiki S, Lee Y, Oba M, Miyata K, Ishii T, et al. pDNA/poly(l-lysine) polyplexes functionalized with a pH-sensitive charge-conversional poly (aspartamide) derivative for controlled gene delivery to human umbilical vein endothelial cells. Macromol Rapid Commun 2010;31(13):1181–6.

[25] Lee Y, Fukushima S, Bae Y, Hiki S, Ishii T, Kataoka K. A protein nanocarrier from charge-conversion polymer in response to endosomal pH. J Am Chem Soc 2007;129:5362–3.

[26] Elgazwy A-SSH. Facile synthesis of (*R*, *R*) and of (*R*, *S*) tricarballylic acid anhydride and imide derivatives. Molecules 2000;5:665–73.

[27] Dinand E, Zloh M, Brocchini S. Competitive reactions during amine addition to *cis*-aconityl anhydride. Aust J Chem 2002;55:467–74.

[28] Sokolova VV, Radtke I, Heumann R, Epple M. Effective transfection of cells with multi-shell calcium phosphate–DNA nanoparticles. Biomaterials 2006;27:3147–53.

[29] Zhang M, Kataoka K. Nano-structured composites based on calcium phosphate for cellular delivery of therapeutic and diagnostic agents. Nano Today 2009;4:508–17.

[30] Sullivan LA, Brekken RA. The VEGF family in cancer and antibody-based strategies for their inhibition. MAbs 2010;2(2):165–75.

[31] Dvorak HF. Vascular permeability factor/vascular endothelial growth factor: a critical cytokine in tumor angiogenesis and a potential target for diagnosis and therapy. J Clin Oncol 2002;20:4368–80.

[32] Boussif O, Lezoualc'h F, Zanta MA, Mergny MD, Scherman D, Demeneix B, et al. A versatile vector for gene and oligonucleotide transfer into cells in culture and *in vivo*: polyethylenimine. Proc Natl Acad Sci U S A 1995;92:7297–301.

Journal of Controlled Release 149 (2011) 51–57

Contents lists available at ScienceDirect

Journal of Controlled Release

journal homepage: www.elsevier.com/locate/jconrel

Antiangiogenic gene therapy of experimental pancreatic tumor by sFlt-1 plasmid DNA carried by RGD-modified crosslinked polyplex micelles

Yelena Vachutinsky [a], Makoto Oba [b], Kanjiro Miyata [c], Shigehiro Hiki [d], Mitsunobu R. Kano [e], Nobuhiro Nishiyama [c,f], Hiroyuki Koyama [b], Kohei Miyazono [e,f], Kazunori Kataoka [a,c,d,f,*]

[a] *Department of Bioengineering, Graduate School of Engineering, The University of Tokyo, 7-3-1 Hongo, Bunkyo-ku, Tokyo 113-8656, Japan*
[b] *Department of Clinical Vascular Regeneration, Graduate School of Medicine, The University of Tokyo, 7-3-1 Hongo, Bunkyo-ku, Tokyo 113-8655, Japan*
[c] *Center for Disease Biology and Integrative Medicine, Graduate School of Medicine, The University of Tokyo, 7-3-1 Hongo, Bunkyo-ku, Tokyo 113-0033, Japan*
[d] *Department of Materials Engineering, Graduate School of Engineering, The University of Tokyo, 7-3-1 Hongo, Bunkyo-ku, Tokyo 113-8656, Japan*
[e] *Department of Molecular Pathology, Graduate School of Medicine, The University of Tokyo, 7-3-1 Hongo, Bunkyo-ku, Tokyo 113-8655, Japan*
[f] *Center for Nano-Bio Integration The University of Tokyo, 7-3-1 Hongo, Bunkyo-ku, Tokyo 113-8656, Japan*

ARTICLE INFO

Article history:
Received 5 October 2009
Accepted 1 February 2010
Available online 6 February 2010

Keywords:
Poly(ethylene glycol)-*block*-poly(L-lysine) (PEG-PLys)
Cyclic RGD peptide
sFlt-1
Antiangiogenic gene therapy
Polyplex micelle

ABSTRACT

Disulfide crosslinked polyplex micelles with RGD peptides were formed through ion complexation of thiolated c(RGDfK)-poly(ethylene glycol)-*block*-poly(L-lysine) (c(RGDfK)-PEG-P(Lys-SH)) and plasmid DNA encoding sFlt-1 and tested for their therapeutic effect in BxPC3 pancreatic adenocarcinoma tumor bearing mice. These micelles, systemically injected, demonstrated significant inhibition of tumor growth up to day 18, as a result of the antiangiogenic effect that was confirmed by vascular density measurements. Significant therapeutic activity of the 15% crosslinked micelle (c(RGDfK)-PEG-P(Lys-SH15)) was achieved by combined effect of increased tumor accumulation, interaction with endothelial cells and enhanced intracellular uptake through receptor-mediated endocytosis. These results suggest that RGD targeted crosslinked polyplex micelles can be effective plasmid DNA carriers for antiangiogenic gene therapy.

1. Introduction

Poly(ethylene glycol) (PEG)-polycation block copolymers have been widely investigated in the field of gene delivery as a potential non-viral vectors for systemic applications [1–7]. The complexes of plasmid DNA (pDNA) and block copolymers form self-assembling particles, termed polyplex micelles, with a core-shell structure. The outer hydrophilic shell layer, formed by PEG segment, increases micelle stability in serum, improves its pharmacokinetic properties, and reduces polymer toxicity [8–11]. Nevertheless, further stabilization and increased longevity in blood are required for polyplex micelles to achieve successful gene delivery *in vivo*.

Disulfide crosslinks were previously introduced into the polyplex micelle core to stabilize its structure in the extracellular entity, while facilitating smooth release of the entrapped pDNA in the intracellular reductive environment [12,13]. Indeed, disulfide crosslinked polyplex micelles exhibited improved transfection of the reporter gene to cultured cells and mouse liver upon systemic administration [13]. In addition, cyclic RGD peptide ligands (c(RGDfK)) were recently installed onto the surface of the disulfide crosslinked polyplex micelles to achieve specific targeting to tumor neo-vasculature [14,15]. RGD (Arg–Gly–Asp) peptide is a recognition motif in multiple ligands of α_v integrin family [16]. Moreover, cyclic RGD peptides showed increased affinity to $\alpha_v\beta_3$ and $\alpha_v\beta_5$ integrin receptors [17] which are overexpressed on tumor angiogenic endothelial cells [18]. Therefore, RGD peptide ligands have been intensively investigated as an active targeting strategy in antiangiogenic gene therapy for cancer [19–22]. Consequently, we hypothesized that polyplex micelles with cyclic RGD ligands and disulfide crosslinks may be a useful system for targeting angiogenic endothelial cells by systemic administration. RGD conjugated polyplex micelles showed remarkably increased transfection efficiency in cultured HeLa cells possessing $\alpha_v\beta_3$ and $\alpha_v\beta_5$ integrins, as a result of increased cellular uptake and intracellular trafficking of micelles toward perinuclear region via caveolae-mediated endocytosis as was previously reported [14,15]. Caveolae- mediated endocytosis is a nondigestive internalization pathway, which does not result in pH decrease, thus avoiding pDNA degradation in acidic organelles in cell. This route might be especially essential for polylysine based pDNA carriers, which do not possess “proton buffering” ability to escape endosome.

Vascular endothelial growth factor (VEGF) is a major proangiogenic molecule, which stimulates angiogenesis via promoting endothelial proliferation, survival and migration [reviewed in [23,24]]. VEGF and VEGF receptors have been found to be up-regulated in

---

[*] Corresponding author. Department of Bioengineering, Graduate School of Engineering, The University of Tokyo, 7-3-1 Hongo, Bunkyo-ku, Tokyo 113-8656, Japan. Tel.: +81 3 5841 7138; fax: +81 3 5841 7139.
E-mail address: kataoka@bmw.t.u-tokyo.ac.jp (K. Kataoka).

0168-3659/$ – see front matter © 2010 Elsevier B.V. All rights reserved.
doi:10.1016/j.jconrel.2010.02.002

various types of tumors and are usually associated with tumor progression and poor prognosis (reviewed in [25]). Inhibition of VEGF or its signaling pathway has been shown to suppress tumor angiogenesis and tumor growth [reviewed in [25–27]].

The soluble form of VEGF receptor-1 (soluble fms-like tyrosine kinase-1: sFlt-1) is a potent endogenous agent for antiangiogenic therapy. The sFlt-1 binds to VEGF with the same affinity and equivalent specificity as that of the original receptor, however inhibits its signal transduction [28–30]. Therefore, exogenous sFlt-1 is considered to be an effective therapeutic agent for antiangiogenic tumor therapy [20,21,31–35]. Recently, several reports were published on *in vivo* non-viral gene therapy with sFlt-1, carried by several types of polymers, for inhibition of tumor angiogenesis [21,35]. Kim WJ et al. reported effective tumor growth suppression in CT-26 colon adenocarcinoma bearing mice by systemic injection of polyethyleneimine based polyplexes, utilizing the RGD targeting approach [21].

In this study, thiolated PEG-poly(L-lysine) (PEG-PLys) block copolymer, combining long PEG chain with optimized crosslinking degree, was designed for construction of RGD-mediated gene delivery system. Here we report the therapeutic effect of sFlt-1 expressing pDNA complexed with 15% thiolated control poly(ethylene glycol)-*block*-poly(L-lysine) (PEG-P(Lys-SH15)) and cyclic RGD conjugated (c(RGDfK)-PEG-P(Lys-SH15)) polymers, forming crosslinked polyplex micelles, after systemic administration to BxPC3 human pancreas adenocarcinoma tumor bearing mice. Note that BxPC3 xenografts are characterized by heterogeneous vascularity and stroma-rich histology [36], which limits access of therapeutic agents to tumor cells. Thus, the accessibility of endothelial cells by bloodstream, makes antiangiogenic approach an attractive strategy against pancreatic tumor.

2. Materials and methods

2.1. Materials

N-Succinimidyl 3-(2-pyridyldithio)-propionate (SPDP) was purchased from Dojindo Laboratories (Kumamoto, Japan). Cyclo[RGDfK(CX-)] (c(RGDfK)) peptides ($X = $ 6-aminocaproic acid: ε-Acp) was purchased from Peptide Institute (Osaka, Japan). The PEG-PLys block copolymer (PEG, 17,000 g/mol; polymerization degree of PLys segment, 73) was synthesized as previously reported [37]. Plasmid DNA coding for luciferase (Luc) under the control of CAG promoter was provided by RIKEN Gene Bank (Tsukuba, Japan), and a fragment cDNA of sFlt-1 was inserted into the pCAcc vector having CAG promoter. The pDNAs were amplified in competent DH5α *Escherichia coli* and purified by the HiSpeed Plasmid Maxi Kit purchased from QIAGEN Sciences Co., Inc. (Germantown, MD). Luc pDNA was labeled with Cy5 by the Label IT Nucleic Acid Labeling Kit (Mirus, Madison, WI) according to the manufacturer's protocol. Dulbecco's modified eagle's medium (DMEM) and fetal bovine serum (FBS) were obtained from Sigma-Aldrich Co (Madison, WI) and Dainippon Sumimoto Pharma Co., Ltd. (Osaka, Japan), respectively. Rat monoclonal antibody to CD31 (platelet endothelial cell adhesion molecule 1 (PECAM1)) was purchased from BD Pharmingen (Franklin Lakes, NJ), and Alexa Fluor 488-conjugated secondary antibody to rat IgG was from Invitrogen Molecular Probes (Eugene, OR).

2.2. Preparation of block copolymers

2.2.1. Synthesis of thiolated PEG-PLys (PEG-P(Lys-SH))

Pyridyldithiopropionyl (PDP) groups were introduced to the ε-amino groups of PLys side chain as reported previously [12]. Briefly, acetal-PEG-PLys (83 mg, 2.86 µmol) was dissolved in 10 mL *N*-methyl-2-pyrrolidone containing 5 wt.% LiCl and stirred with a heterobifunctional reagent, SPDP, (10 mg, 31 µmol) in the presence of *N,N*-diisopropylethylamine (10 mol excess against the SPDP reagent) for 3 h at room temperature. The mixture was then precipitated into 20 times excess volume of diethyl ether. The precipitated polymer was dissolved in 10 mM phosphate buffer (pH 7.0, 150 mM NaCl), dialyzed against the same buffer and then distilled water, and lyophilized to obtain PEG-P(Lys-PDP). The degree of PDP substitution for each polymer was determined from the peak intensity ratio of the methylene protons of PEG (OCH_2CH_2, $\delta = 3.5$ ppm) to the pyridyl protons of the 3-(2-pyridyldithio)propionyl group (C_5H_4N, $\delta = 7.2$–8.3 ppm) in the ^1H NMR spectrum (D_2O, 25 °C). Block copolymer with X % thiolation degree was abbreviated as B-SHX%.

2.2.2. Synthesis of c(RGDfK)-PEG-P(Lys-SH)

Acetal-PEG-P(Lys-PDP) (30 mg, 1 µmol) was dissolved in 10 mM Tris–HCl buffer solution (pH 7.4) (3 mL) with 10 eq. of dithiothreitol (DTT). After 30 min incubation at room temperature, the polymer solution was dialyzed against 0.2 M AcOH buffer (pH 4.0). c[RGDfK(CX-)] (8 mg, 6.5 mmol) in AcOH buffer (3 mL) was then added to the polymer solution. After stirring for 5 days, DTT (6.67 mg, 43.9 µmol) was added and stirred at room temperature for 3 h. The reacted polymer was purified by dialysis sequentially against 10 mM phosphate buffer pH 7.0 with 150 mM NaCl and distilled water, and lyophilized to obtain c(RGDfK)-PEG-P(Lys-SH) [14].

2.3. Preparation of polyplex micelles

The above polymers were dissolved in 10 mM Tris–HCl buffer (pH 7.4) containing 10% volume of 100 mM DTT. After 30 min at ambient temperature, twice-excess volume of pDNA solution (50 µg/mL) in the same buffer was added to the polymer solution to form a polyplex micelle at *N*/*P* ratio of 2. The *N*/*P* ratio was defined as the residual molar ratio of amino groups of thiolated PEG-PLys to phosphate groups of pDNA. After an overnight incubation at ambient temperature, the polyplex micelle solutions were dialyzed against 10 mM Tris–HCl (pH 7.4) containing 0.5% dimethylsulfoxide (DMSO) at 37 °C for 24 h, followed by additional 2 days dialysis for the DMSO removal. During these dialysis processes, thiol groups of the polymers in the micelles were oxidized to form disulfide crosslinks. The concentration of pDNA in each micelle solution was determined by absorbance at 260 nm. Polyplex micelles with and without cyclic RGD peptide ligands were abbreviated as RGD(+) and RGD(−), respectively.

2.4. Quantitative determination of transfection efficiency by real time reverse transcription-polymerase chain reaction (RT-PCR) for sFlt-1

HeLa cells, expressing the $\alpha_v\beta_3$ and $\alpha_v\beta_5$ integrin receptors, were seeded on 24-well culture plates (10000 cells/well) and incubated for 24 h in 500 µL of DMEM medium containing 10% FBS. Micelle solutions were then added at a concentration equivalent to 1 µg of pDNA per well and the cells were incubated for 48 h. Following this incubation period, total RNA was extracted from the cells and transcripted to cDNA. The cDNA samples were subjected to polymerase chain reaction (PCR) amplification using the following human specific primers: 5′-CCACTCCCTTGAACACGAG-3′ and 3′-CGCCTTACGGAAGCTCTCT-5′. Amplification conditions were as recommended by the manufacturer (QIAGEN Sciences Co., Inc.). Unknown and standard samples were run in triplicate. Concentrations of unknown samples were interpolated from a standard curve, established by simultaneous amplification of sFlt-1 plasmid standards.

2.5. In vivo studies

2.5.1. Mice

Five-week-old female Balb/c nude mice were purchased from Charles River Laboratories (Tokyo, Japan). Mice were maintained on ad libitum rodent feed and water. The experimental animals were allowed to acclimate for at least 1 week before tumor implantation. All studies were performed in accordance to the Guide for the Care and Use of Laboratory Animals as stated by the National Institutes of Health.

2.5.2. Tumor implantation

BxPC3 cell line (ATCC, Manassas, VA), derived from human pancreatic tumor was inoculated to nude mice subcutaneously to develop xenografts (100 μl of 5×10^7 cells/mL PBS suspension). Tumors were allowed to grow for 3 weeks till their size reached approximately 120–160 mm^3.

2.5.3. Blood circulation

Polyplex micelles loading Cy5-labeled pDNA (100 μg pDNA/mL, 200 μL) were intravenously injected to the mice via the tail vein at a dose of 20 μg pDNA/mouse. Blood was collected from the postcaval vein under anesthesia 15 min after injection and centrifuged to obtain blood plasma. Two microliters of 10X trypsin-EDTA were added to 20 μL of the plasma and incubated overnight at 37 °C to release pDNA from the micelle by digesting PLys segment of the block copolymer. The fluorescence intensity of the sample solution was measured at $\lambda = 670$ nm by spectrofluorometer (ND-3300, Nano Drop, Wilmington, DE), and percent of pDNA dosage in the blood was calculated according to the following equation:

$$\%\ \text{injected pDNA in the blood} = (F_{670(\text{sample})} / F_{670(\text{control})}) \times 100 \quad (1)$$

where the $F_{670(\text{control})}$ represents the fluorescence intensity of micelle solution mixed with blood sample (time 0).

2.5.4. In vivo tumor growth inhibition

Polyplex micelles, loading pDNA equivalent to 20 μg and dissolved in 10 mM Hepes buffer (pH 7.4) with 150 mM NaCl, were administered intravenously on days 0, 4, and 8. Tumor size was measured every 2 days by a digital vernier caliper across its longest (a) and shortest diameters (b) and its volume (V) was calculated according to the formula $V = 0.5ab^2$. Tumor progression was evaluated in terms of relative tumor volume (to day 0) over a period of 18 days.

2.5.5. Quantification of microvessel density

At the end of *in vivo* tumor growth studies, xenografted tumors were excised and frozen in tissue-Tek-OCT. The frozen tumors were cut into 10 μm thick slices with a cryostat maintained at −23 °C. Vascular endothelial cells were immunostained by incubation of the cryosections with anti-CD31 antibody followed by incubation with Alexa Fluor 488-conjugated secondary antibody. The tumor cryosections were observed by a confocal laser scanning microscope (CLSM), LSM 510 (Carl Zeiss, Oberlochen, Germany). Microvessel density was quantified by counting the percentage area of CD31 positive pixels per image with at least 21 images per sample (i.e., three animals per sample x 7 cryosections per tumor).

2.5.6. Micelle accumulation in tumor tissue

Polyplex micelles loading Cy5-labeled pDNA were intravenously injected at a dose of 20 μg pDNA/mouse. Mice were sacrificed after 24 h and the excised tumors were fixed in formalin for 1 h, followed by 1 h incubation periods with 10, 15 and 20% sucrose/PBS solutions at room temperature. The tumors were frozen in tissue-Tek-OCT and cryosections were prepared for CLSM visualizations as described in the previous section. The nuclei were stained with Hoechst 33342 (Dojindo Lab., Kumamoto, Japan). The CLSM observations were performed at the excitation wavelengths of 488 nm (Ar laser) for the Alexa Fluor 488, 633 nm (He–Ne laser) for Cy5, and 710 nm (MaiTai laser, two photon excitation) for Hoechst 33342, respectively. The percentage of pDNA positive pixels per image was counted to quantify the micelle accumulation inside the tumor tissue.

2.6. Data analysis

The experimental data was analyzed by Student's *t*-test. $P<0.05$ was considered as significant.

3. Results

Thiolated acetal-PEG-PLys block copolymers, composed of 17 kDa M.W. PEG and 73 lysine units, were prepared as described elsewhere [12,14,37]. SPDP was used as a thiolating reagent and conjugated to the ε-amino group of lysine unit. Conjugation of c (RGDfK) peptide ligands into the PEG terminus of acetal-PEG-P(Lys-PDP) was achieved through the formation of a thiazolidine ring between the *N*-terminal cysteine and the aldehyde group converted from the acetal group [14,15]. The targetable polyplex micelles were prepared through ion complexation of the above polymers with pDNA at $N/P = 2$ (Fig. 1), and analyzed for their size and ζ-potential by DLS and laser-doppler electrophorsis, respectively. The cumulant diameters of the B-SHX% micelles were approximately 104 ± 18 nm, with a moderate polydispersity index of 0.2. The ζ-potentials were found to be approximately 0.5 mV, as a result of the PEG palisade formation surrounding the polyplex core [8,14].

Following *in vitro* transfection in HeLa cells, the mRNA expressions of sFlt-1 were quantitatively analyzed by real time RT-PCR. From this analysis, presented in Fig. 2, it is clear that the cells were successfully transfected by the polyplex micelles. The highest transfection efficiency was achieved by RGD(+) B-SH15% crosslinked (15(+)) micelle. Worth noting, detectable protein level of sFlt-1 by ELISA, specific to human VEGF-R1/sFlt-1 (R&D Systems), could be achieved for this formulation only (1.2 ± 0.05 ng/mL) (data not shown). Other micelles, probably, resulted in sFlt-1 levels which are beyond the sensitivity of this assay (<13 pg/ml). The increased transfection efficiency of the 15(+) micelle results from the combination of crosslinked core and receptor targeting ligand, consistent with our previous studies [15].

The blood circulation experiments were carried out in BxPC3 tumor bearing mice upon intravenous injections of the Cy5-labeled pDNA (20 μg pDNA/ mouse). Blood was collected from the postcaval vein 15 min after administration and analyzed for its fluorescence intensity. Disulfide crosslinks prolonged blood circulation time, while the RGD conjugation resulted in significantly lower blood circulation period of polyplex micelles, as shown in Fig. 3. In the case of crosslinked system, 28% and 21% of injected pDNA were observed in plasma for RGD(−) and RGD(+) micelles, respectively. Significantly lower recovered doses of pDNA, 11 % and 7 % for RGD(−) and RGD(+) micelles, respectively, were found for non crosslinked system. We further evaluated micelle accumulation in tumor by iv administration of RGD-conjugated or non-conjugated 15% crosslinked micelles prepared with Cy5-labeled pDNA at a dose of 20 μg pDNA/mouse. Both micelles were found to be localized in the tumor blood vessels, 24 h after administration, as was indicated by colocalization of the Cy5-labeled pDNA (red) and the CD31 positive endothelial cells (green) (Fig. 4A). However, quantitative analysis of the pDNA positive area per image revealed significantly higher accumulation of the RGD-conjugated micelle than non-conjugated micelle inside the tumor tissue (Fig. 4B): 3.08 % and 2.44 % of red pixels per image for RGD(+) and RGD(−) micelle, respectively ($P<0.05$).

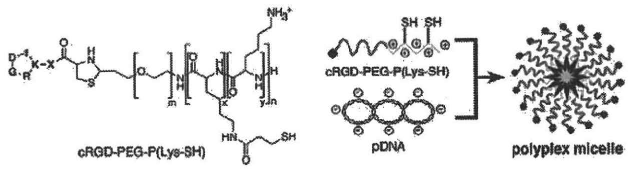

Fig. 1. Structure of cRGD-PEG-P(Lys-SH) and its polyplex micelle.

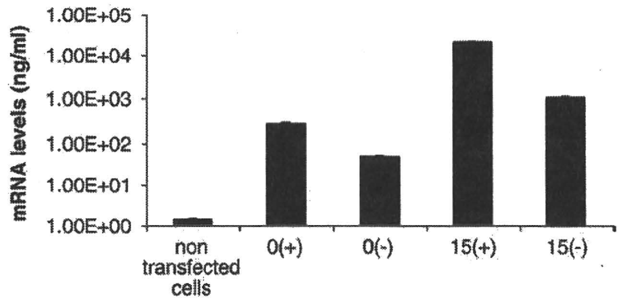

Fig. 2. *In vitro* transfection efficiency of sFlt-1 plasmid DNA in HeLa cells. The cells were transfected with RGD(+) and RGD(−) non crosslinked micelles (0(+) and 0(−)) and RGD(+) and RGD(−) 15% crosslinked micelles (15(+) and 15(−)), respectively. Non transfected cells were used as control. Each well was transfected with 1 μg of pDNA for 48 h and analyzed for sFlt-1 mRNA levels by real time RT-PCR.

The therapeutic effect of polyplex micelles following intravenous administration of the sFlt-1 expressing pDNA was evaluated by tumor growth inhibition study in BxPC3 tumor bearing mice. When tumors reached the volume of 120–160 mm^3, animals were injected with three doses of polyplex micelles containing either sFlt-1 or Luc expressing plasmid (20 μg pDNA/dose) on days 0, 4 and 8. The results of these studies, in terms of relative tumor volumes (Fig. 5), indicate the ability of RGD(+) and RGD(−) crosslinked polyplex micelles as vehicles for therapeutic gene delivery in BxPC3 tumor bearing mice. In the case of animals treated with 15(+) micelles, the tumor progression was significantly inhibited from day 6, compared to control mice. By the end of the experiment, the mean tumor volume in this group was 1.67 ± 0.18 of initial tumor volume. In the group of animals treated with pDNA encapsulated in RGD(−) micelles, significant inhibition of tumor progression was observed only from day 12, and the mean tumor volume reached 1.93 ± 0.52 of initial tumor volume by the end of the experiment. On the other hand, tumors grew much faster in the control groups, and reached 2.58 ± 0.5 of initial tumor volume.

Intravenous administration of crosslinked polyplex micelles containing sFlt-1 pDNA to BxPC3 tumor bearing mice resulted in significant reduction in the tumor neo-vasculature, as shown by CD31 immunostaining of the tumor cryosections. Representative images are shown in Fig. 6A. Increased density of blood vessels throughout the tissue was observed in control tumors. In contrast, very few blood vessels could be observed in the sFlt-1 treated groups. The quantitative results of microvessel density in tumor tissue cryosections were obtained by counting the area of stained blood vessels (green pixels) per image (Fig. 6B). Systemic administration of sFlt-1 expressing pDNA in the RGD(+) micelles resulted in the lowest average microvessel density of only 8.6% per image, whereas the RGD (−) micelle carrying pDNA led to 12.3% vessels per image. The control group had an average microvessel area of 23.7% per image, significantly higher as compared to the treated groups.

4. Discussion

In this study, we demonstrate that crosslinked polyplex micelles formed by electrostatic interaction of thiolated PEG-PLys block copolymers, modified on their surface with cRGD peptide ligand, and sFlt-1 pDNA are effective for *in vivo* tumor regression upon systemic administration. The thiolated PEG-PLys block copolymer, in this study, was further optimized by higher molecular weight PEG (17,000 Da) against 12,000 Da M.W. PEG used so far [2,3,8,12–15], to achieve enhanced shielding effect and thus higher stability in blood. Block copolymer with 15% thiolation degree, which showed the highest transfection efficiency *in vitro* and *in vivo* (data not shown), was selected for construction of RGD-mediated gene delivery vector.

The results of sFlt-1 transfection in Hela cells show higher mRNA expression levels in the cells transfected by RGD(+) crosslinked micelle relative to either RGD(−) or non crosslinked micelles (Fig. 2). This result is consistent with our previous studies, indicating the greater stability of crosslinked micelles in the medium and specific affinity of RGD ligand to $\alpha_v\beta_3$ and $\alpha_v\beta_5$ integrin receptors expressed in HeLa cells [14,15]. Micelle internalization to the cell via integrin-mediated endocytosis contributes to the accelerated accumulation of pDNA in the perinuclear region through the change in its intracellular trafficking from clathrin-mediated to caveolae-mediated endocytosis, resulting in enhancement of gene expression [15].

When administrated intravenously into BxPC3 tumor bearing mice, blood levels of Cy5-labeled pDNA were significantly lower for the RGD(+) micelle compared to the RGD(−) micelle. This observation might be partly explained by enhanced accumulation of pDNA in tumor site when carried by RGD(+) micelle over RGD(−) (Fig. 4B) and other organs as well. These observations are in good agreement with other works using cyclic RGD-modified particles, which reported significantly lower blood circulation times [38–40] while higher accumulation in tumor tissue [21,38–41], liver [21,38–42] and spleen [28–31] compared to the control. Moreover, CLSM observations demonstrated colocalization of both micelles with tumor endothelial cells, confirming their potential as effective antiangiogenic gene delivery vehicles (Fig. 4A).

In vivo tumor growth assay revealed significant ($P<0.05$) tumor growth inhibition when the sFlt-1 pDNA was administrated by crosslinked micelles as compared to control groups. Compared to RGD(−), the RGD(+) micelle was more effective in suppressing tumor growth. The significant difference in relative tumor volumes between RGD(+) injected and control groups was observed from day 6 till the end of the experiment. In comparison, significant difference between RGD(−) injected and control groups was observed only from day 12. In addition, relative tumor volumes in the RGD(+) injected group were lower than those in the RGD(−). These findings may be explained by greater tumor accumulation and higher transfection efficiency of RGD-modified micelle, resulted from more effective intracellular plasmid delivery through specific receptor binding and endocytosis. The lack of significant difference in relative tumor volumes between the RGD(+) and RGD(−) injected groups might be due to the lower circulation time in blood of the RGD(+) micelle and its enhanced accumulation in organs such as liver and spleen. Accumulation in liver [21,38–42] and spleen [39–42] was shown for various cyclic RGD-modified vectors and was, in general, attributed to their accelerated clearance through the phagocytosis by macrophages located on reticuloendothelial system (RES) [39–41].

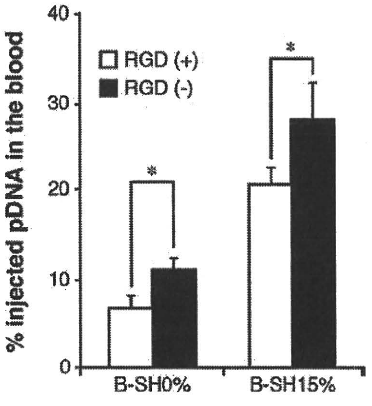

Fig. 3. Blood circulation of plasmid DNA carried by RGD (+/−) polyplex micelles. Micelles loading Cy5-labeled pDNA were intravenously administrated to the tumor bearing mice (20 μg pDNA/mouse). Blood was collected 15 min after administration and analyzed for its fluorescence intensity. $N=3$, Mean ± s.d. $^{*}P<0.05$ compared to RGD(−).

The antiangiogenic effect of expressed sFlt-1 was confirmed by CD31 immunostaining of the tumor cryosections and quantification of microvessel density. From these studies, it is clear that sFlt-1 was able to significantly suppress tumor neo-vasculature formation when the pDNA was delivered in RGD(+) and RGD(−) crosslinked micelles. The most pronounced effect on microvessel density was observed with the plasmid administrated in RGD(+) micelles. This is probably due to the combined effect of tumor accumulation and increased transfection efficiency of the RGD-conjugated 15% crosslinked polyplex micelle.

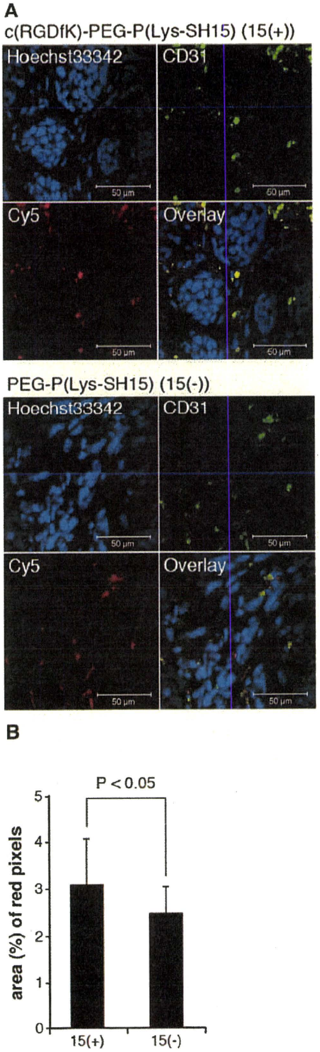

Fig. 4. Micelle localization in tumor tissue. (A) Tumor endothelium and pDNA localization. Immunostaining of CD31 (green) revealed colocalization of Cy5-labeled pDNA (red) with tumor vasculature for both RGD-conjugated (15(+)) and non-conjugated (15(−)) micelles, 24 h after administration. The cell nuclei were stained with Hoechst 33342 (blue). (B) Quantitative analysis of Cy5-labeled pDNA (red pixels). The results represent percentage areas of pDNA-positive pixels per image. Seven images were taken from each tumor tissue, from 3 mice, mean ± s.d.

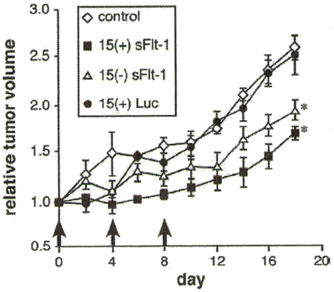

Fig. 5. *In vivo* tumor growth inhibition. RGD (+) and RGD (−) 15% crosslinked polyplex micelles loading plasmid DNA coding either sFlt-1 or Luc were administrated intravenously to BxPC3 tumor bearing mice at a pDNA dose of 20 µg on days 0, 4 and 8, as indicated by arrows. Control animals were injected with either Hepes buffer or 15 (+) micelle loading Luc expressing pDNA. Tumor volumes were measured every 2 days up to day 18 and normalized to the initial tumor volume (day 0). Results are presented in terms of relative tumor volumes, mean ± s.d., $N=6$. *$P<0.05$ compared to control group.

5. Conclusion

Our data contributes to the list of successful non-viral systems for antiangiogenic cancer gene therapy utilizing sFlt-1 pDNA as VEGF sequester [21,35] and RGD targeting of tumor endothelial cells [19,21]. Worth noting, the antiangiogenic gene therapy by sFlt-1 pDNA, delivered by non-viral vector with cRGD ligand, appears to be a promising strategy to treat an intractable pancreatic tumor.

The significant inhibitory effect of tumor growth shown in this study, confirms the potential of c(RGDfK)-PEG-P(Lys-SH15) and PEG-P(Lys-SH15) polyplex micelles as effective systemic gene delivery systems to the neo-vasculature of solid tumors. Both of these formulations showed accumulation and interaction with tumor endothelial cells. The therapeutic activity of c(RGDfK)-PEG-P(Lys-SH15) was pronounced by combined effect of increased tumor accumulation and enhanced intracellular delivery. Based on these studies, c(RGDfK)-PEG-P(Lys-SH15) can be employed as an effective platform for systemic administration of therapeutic plasmid DNA for antiangiogenic therapy.

Acknowledgement

This work was financially supported in part by the Core Research Program for Evolutional Science and Technology (CREST) from Japan